JEM Journal of Experimental Medicine

ARTICLE

A crucial role for Jagunal homolog 1 in humoral immunity and antibody glycosylation in mice and humans

Astrid Hagelkruys[1], Gerald Wirnsberger[1,2], Johannes Stadlmann[1,3], Miriam Wöhner[4], Marion Horrer[1], Bojan Vilagos[5], Gustav Jonsson[1], Melanie Kogler[1], Luigi Tortola[1,6], Maria Novatchkova[4], Peter Bönelt[4], David Hoffmann[1], Rubina Koglgruber[1], Ulrike Steffen[7], Georg Schett[7], Meinrad Busslinger[4], Andreas Bergthaler[5], Christoph Klein[8], and Josef M. Penninger[1,9]

Jagunal homolog 1 (JAGN1) has been identified as a critical regulator of neutrophil biology in mutant mice and rare-disease patients carrying *JAGN1* mutations. Here, we report that *Jagn1* deficiency results in alterations in the endoplasmic reticulum (ER) of antibody-producing cells as well as decreased antibody production and secretion. Consequently, mice lacking *Jagn1* in B cells exhibit reduced serum immunoglobulin (Ig) levels at steady state and fail to mount an efficient humoral immune response upon immunization with specific antigens or when challenged with viral infections. We also demonstrate that *Jagn1* deficiency in B cells results in aberrant IgG N-glycosylation leading to enhanced Fc receptor binding. *Jagn1* deficiency in particular affects fucosylation of IgG subtypes in mice as well as rare-disease patients with loss-of-function mutations in *JAGN1*. Moreover, we show that ER stress affects antibody glycosylation. Our data uncover a novel and key role for JAGN1 and ER stress in antibody glycosylation and humoral immunity in mice and humans.

Introduction

The humoral branch of the immune system is responsible for the production of circulating antibodies to remove pathogens and harmful molecules. Following antigen exposure, naive B lymphocytes recognize cognate antigens with their B cell receptor and upon provision of appropriate costimulatory signals differentiate into memory B cells and plasma cells, which secrete thousands of antibodies per cell per second (Hibi and Dosch, 1986). These exceptionally high rates of Ig production and secretion are enabled by structural reorganization and extensive generation of the ER and Golgi apparatus during B cell differentiation into plasma cells (Wiest et al., 1990). The ER is a cellular organelle responsible for protein folding and assembly, lipid and sterol synthesis, and calcium storage and is positioned adjacent to the Golgi apparatus, which processes proteins for secretion, e.g., by extensive protein glycosylation (Kornfeld and Kornfeld, 1985).

Ig are secreted glycoproteins that recognize antigens via their antigen-binding fragment regions. Additionally, Ig communicate with other components of the immune system via their fragment crystallizable (Fc) region to exert their effector functions (Huber et al., 1976; Woof and Burton, 2004). The Fc domain of Ig can also interact with complement proteins (Miletic and Frank, 1995). Both the antibody isotype determined by the constant, heavy chain (CH) region as well as the pattern of N-glycosylation are important determinants of antibody functionality (Stavnezer et al., 2008; Tao and Morrison, 1989). Antibody glycans are assembled and attached mainly to asparagine 297 (Asn297) of the CH2 domain of the IgG antibody polypeptide chain in the ER and further modified during passage through the Golgi apparatus. The N-linked glycosylation of an IgG antibody has been shown to affect its conformation and thereby its capacity to interact with Fc receptors on cells of the innate immune system (Vidarsson et al., 2014; Arnold et al., 2007). This can affect both an antibody's half-life as well as modulate its effector functions (Jennewein and Alter, 2017). These glycosylation-modulated interactions enable immune responses including antibody-dependent cell-mediated cytotoxicity (ADCC),

[1]Institute of Molecular Biotechnology of the Austrian Academy of Sciences, Vienna, Austria; [2]Apeiron Biologics AG, Vienna, Austria; [3]Institute of Biochemistry, University of Natural Resource and Life Sciences, Vienna, Austria; [4]Research Institute of Molecular Pathology, Vienna Biocenter, Vienna, Austria; [5]CeMM Research Center for Molecular Medicine of the Austrian Academy of Sciences, Vienna, Austria; [6]Institute of Molecular Health Sciences, ETH Zurich, Zurich, Switzerland; [7]Department of Internal Medicine 3-Rheumatology and Immunology, Friedrich-Alexander-University Erlangen-Nürnberg and Universitätsklinikum Erlangen, Erlangen, Germany; [8]Department of Pediatrics, Dr. von Hauner Children's Hospital, Ludwig Maximilians University, Munich, Germany; [9]Department of Medical Genetics, Life Science Institute, University of British Columbia, Vancouver, Canada.

Correspondence to Josef M. Penninger: josef.penninger@imba.oeaw.ac.at; Astrid Hagelkruys: astrid.hagelkruys@imba.oeaw.ac.at.

antibody-dependent cellular phagocytosis, complement-dependent cytotoxicity (CDC), or neutrophil activation (Nimmerjahn and Ravetch, 2008; Kellner et al., 2017). Insights into the role of glycosylation in the regulation of antibody-mediated immune functions have been applied to glyco-engineer therapeutic monoclonal antibodies to enhance or alter their effector functions (Jefferis, 2009). Moreover, alterations in antibody glycosylation have been linked to autoimmunity (Seeling et al., 2017). However, the in vivo molecular control and regulation of a B cell's cellular adaptation to high rates of antibody production, glycosylation, and secretion remains poorly understood.

Jagn1 encodes a ubiquitously expressed transmembrane protein that has been demonstrated to be essential for both ER reorganization in *Drosophila melanogaster* oocyte development (Lee and Cooley, 2007) and more recently the differentiation and survival of human neutrophils (Boztug et al., 2014). Thus far, described defects in mammals have been limited to neutrophils, where JAGN1 regulates the process of granule formation (Boztug et al., 2014; Wirnsberger et al., 2014). Since differentiation of B cells into antibody-secreting plasma cells involves a significant ER expansion to support high rates of antibody production and secretion, we set out to study a role for JAGN1 in B cell biology. Here we report that loss of *Jagn1* in B cells causes defects in Ig production and secretion as well as aberrant IgG glycosylation and subsequent enhanced Fc receptor binding. Our data uncover a novel role for JAGN1 in B cell biology to critically regulate humoral immunity in mice and humans.

Results

Deletion of *Jagn1* in B cells results in decreased Ig levels and impaired humoral immunity

To study a role for *Jagn1* in B cells, we bred *Jagn1*$^{fl/fl}$-*Mb1*-Cre mice (hereafter referred to as *Jagn1*$^{\Delta B}$) to delete *Jagn1* at the early pro–B cell stage (Hobeika et al., 2006). To exclude Cre effects in the *Mb1*-Cre line, we analyzed B cell development and B cell subset composition as well as serum Ig levels in *Mb1*-Cre and control littermates. We did not observe any significant differences between those cohorts in all parameters tested (Fig. S1, A–C) and therefore used *Jagn1*$^{fl/fl}$ mice as controls throughout the manuscript. Efficient deletion of *Jagn1* in the B cell lineage was determined by measuring *Jagn1* mRNA levels in B220^{+} splenic B cells and in vitro–differentiated plasmablasts (Fig. S2 A). Protein loss was confirmed by intracellular staining for JAGN1 in plasma cells using flow cytometry (Fig. S2 B). To assess the subcellular localization of JAGN1 in B cells, we next established a plasmacytoma cell line (MPC-11) by knockdown of endogenous *Jagn1* and expression of JAGN1 fused to an amino-terminal V5 tag. Immunohistochemical analysis revealed that V5-JAGN1 localized to the ER in B cells (Fig. S2 C).

To assess B cell function, serum Ig levels of *Jagn1*$^{\Delta B}$ mice and control *Jagn1*$^{fl/fl}$ littermates were measured by immunoassays using the Luminex xMAP technology. *Jagn1*$^{\Delta B}$ mice exhibited an isotype-dependent 4–18-fold reduction in serum Ig levels in unchallenged mice (Fig. 1 A). We next assessed the role of JAGN1 in the generation of antigen-specific humoral immune responses. *Jagn1*$^{\Delta B}$ mice displayed significantly reduced titers of OVA-specific IgG and IgM antibodies after immunization with OVA/alum when compared with littermate control mice (Fig. 1 B). Consistent with impaired anti-OVA responses, *Jagn1*$^{\Delta B}$ mice immunized with the hapten NP (4-hydroxy-3-nitrophenyl-acetyl) coupled to the carrier protein KLH also showed a striking reduction in the generation of NP-specific IgG1 antibody–secreting cells, as assessed by ELISPOT (Fig. 1 C). The profound defects in humoral immunity in *Jagn1*$^{\Delta B}$ mice prompted us to study their B cell response in a physiologically relevant immune response upon infection with vesicular stomatitis virus (VSV; Turner et al., 2008). Upon infection with VSV, *Jagn1*$^{\Delta B}$ mice exhibited significantly decreased titers of virus-specific total Ig and, even more pronounced, of antiviral IgG antibodies (Fig. 1 D). These data show that deletion of *Jagn1* in the B cell lineage results in decreased Ig levels in naive mice and strongly diminished humoral responses upon immunization with specific antigens or when challenged with a viral infection.

Jagn1 deficiency impairs plasma cell development

To gain insight into the role of *Jagn1* in B cell development and homeostasis, we analyzed steady-state levels of developmental and mature B cell subpopulations in the bone marrow (BM) and spleen of *Jagn1*$^{\Delta B}$ and control littermate mice by flow cytometry. *Jagn1*$^{\Delta B}$ mice showed apparently normal early B cell development but exhibited markedly reduced levels of BM plasma cells (Lin^{-}CD28^{+}CD138^{+}) when compared with littermate control mice (Fig. 2 A). While we observed a marked effect of *Jagn1* deficiency on the plasma cells residing in the BM, which are long-lived and the major source of serum antibody levels (Benner et al., 1981; Slifka et al., 1995; Manz et al., 1997; Slifka et al., 1998), short-lived plasma cells in the spleen (Lin^{-}CD28^{+}CD138^{+}) were only slightly reduced in *Jagn1*$^{\Delta B}$ mice (Fig. 2 B). Additionally, *Jagn1*$^{\Delta B}$ mice exhibited enlarged spleens, increased proportions of splenic marginal zone (MZ; CD21^{+}CD23^{low}) B cells, and reduced proportions of follicular (FO; CD23^{+}CD21^{int}) B cells, as detected by flow cytometric analyses and immunohistochemistry, when compared with littermate control mice (Fig. 2, B and C; and Fig. S2 D). Thus, inactivation of *Jagn1* results in markedly impaired BM plasma cell numbers and altered splenic B cell populations.

To investigate B cell–intrinsic effects of *Jagn1* deletion, we generated mixed BM chimeric mice. To this end, we transplanted a 1:1 mixture of enhanced GFP–labeled (*Rosa26*-EGFP) *Jagn1*$^{+/+}$ BM plus *Jagn1*$^{fl/fl}$ or *Jagn1*$^{\Delta B}$ BM into lethally irradiated *Rag2*$^{-/-}$ recipient mice. The increased MZ/FO B cell ratio observed in *Jagn1*$^{\Delta B}$ mice was restored to control levels in *Jagn1*$^{\Delta B}$ BM–derived cells by the presence of wild-type cells (Fig. 2 D). Moreover, in these mixed BM chimeric mice, the presence of *Jagn1*$^{+/+}$ B cells also restored serum IgM to levels observed in control BM chimeric animals (Fig. 2 E). These data indicate that the increased numbers and proportions of MZ B cells observed in *Jagn1*$^{\Delta B}$ mice are not caused by an intrinsic function of JAGN1 in MZ B cell differentiation or homeostasis but are a secondary effect, most probably caused by reduced Ig serum levels (Tsiantoulas et al., 2017). While *Jagn1*$^{fl/fl}$ and *Jagn1*$^{\Delta B}$ BM–derived cells equally contributed to the reconstitution of mature splenic B cell populations (Fig. 2 F), *Jagn1*$^{\Delta B}$ BM–derived cells were

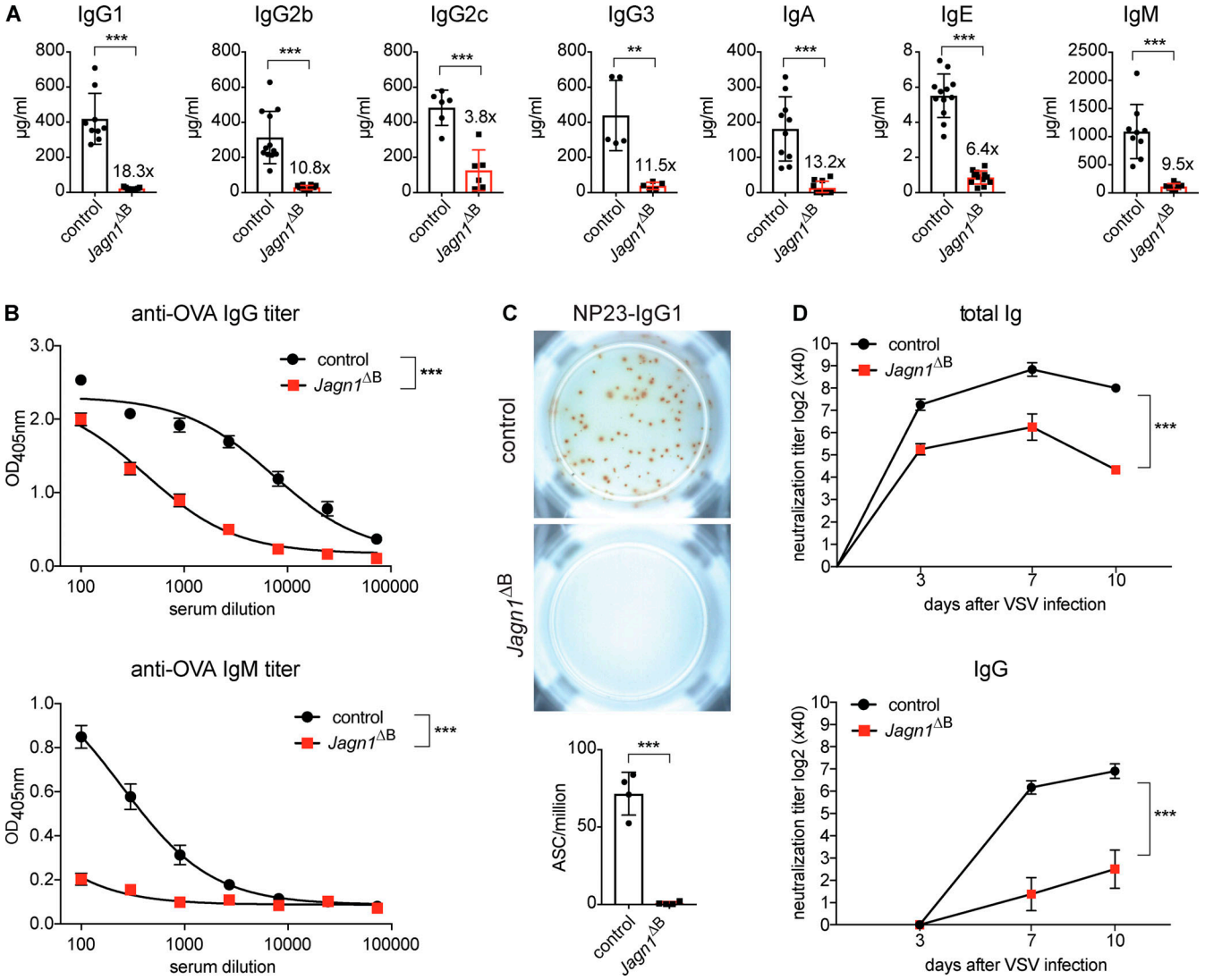

Figure 1. **Decreased Ig levels in naive, immunized, and VSV-infected *Jagn1*$^{\Delta B}$ mice. (A)** Ig concentrations in sera from control *Jagn1*$^{fl/fl}$ and *Jagn1*$^{\Delta B}$ mice as assessed with an isotype-multiplexing assay (n > 4). Fold reductions are indicated above bar diagrams. Data are shown for one of three independent experiments. **(B)** Control *Jagn1*$^{fl/fl}$ and *Jagn1*$^{\Delta B}$ mice were immunized with OVA/alum, and IgG (upper panel) and IgM (lower panel) titers were measured by ELISA 14 d later (n > 2). Data are shown for one of two independent experiments. **(C)** Control *Jagn1*$^{fl/fl}$ and *Jagn1*$^{\Delta B}$ littermate mice were immunized with NP-KLH/alum, and splenic B cells were analyzed 14 d later. Upper panel depicts ELISPOT analysis, and lower panel depicts quantification of NP23-specific IgG1 antibody–secreting cells (ASC) of one million seeded cells (n = 4). Data are shown for one of two independent experiments. **(D)** Control *Jagn1*$^{fl/fl}$ and *Jagn1*$^{\Delta B}$ mice were infected with VSV, and titers of virus-specific neutralizing total Ig (upper panel) and IgG (lower panel) antibodies were measured by a virus plaque neutralization test at day 3, 7, and 10 after infection (n > 3). Data are shown for one of three independent experiments. For panels A and C, each data point represents an individual mouse. P values were calculated using the Student's t test. Panels B and D were analyzed by two-way ANOVA with Bonferroni correction. **, P < 0.01; ***, P < 0.001. Error bars represent means ± SD.

depleted in CD28$^+$CD138$^+$ plasma cells both in the spleen and the BM (Fig. 2 G). To further characterize the plasma cell phenotype, we crossed *Jagn1*$^{\Delta B}$ mice to *Blimp1*-GFP reporter mice (Kallies et al., 2004), carrying a GFP reporter gene in the *Blimp1* locus. The transcription factor BLIMP1 is a central regulator of plasma cell differentiation (Tellier et al., 2016; Minnich et al., 2016). This allowed for the detection of CD138$^+$GFP$^+$ plasma cells irrespective of their CD28 expression status and confirmed that *Jagn1*$^{\Delta B}$ mice indeed exhibit severely reduced numbers and proportions of BM plasma cells with lower levels of BLIMP1-GFP per cell (Fig. S2 E). In addition to their decreased numbers, the remaining *Jagn1*-deficient plasma cells exhibited significantly lower levels of IgM on a per-cell basis as shown by intracellular staining and analysis by flow cytometry (Fig. S2 F). Moreover, intracellular staining revealed reduced BLIMP1 protein levels in *Jagn1*$^{\Delta B}$ plasma cells (Fig. S2 G). These data indicate that loss of *Jagn1* results in a competitive disadvantage to generate plasma cells.

To account for possible early developmental defects contributing to the observed plasma cell phenotype in the *Jagn1*$^{\Delta B}$ animals, we generated *Jagn1*$^{fl/fl}$-*Cd23*-Cre mice to delete *Jagn1* at a later developmental stage (Kwon et al., 2008). In these mice, we detected a phenotype similar to the one observed for *Mb1*-Cre–mediated *Jagn1* deletion, although slightly weaker for BM plasma cells (Fig. S1, D–F).

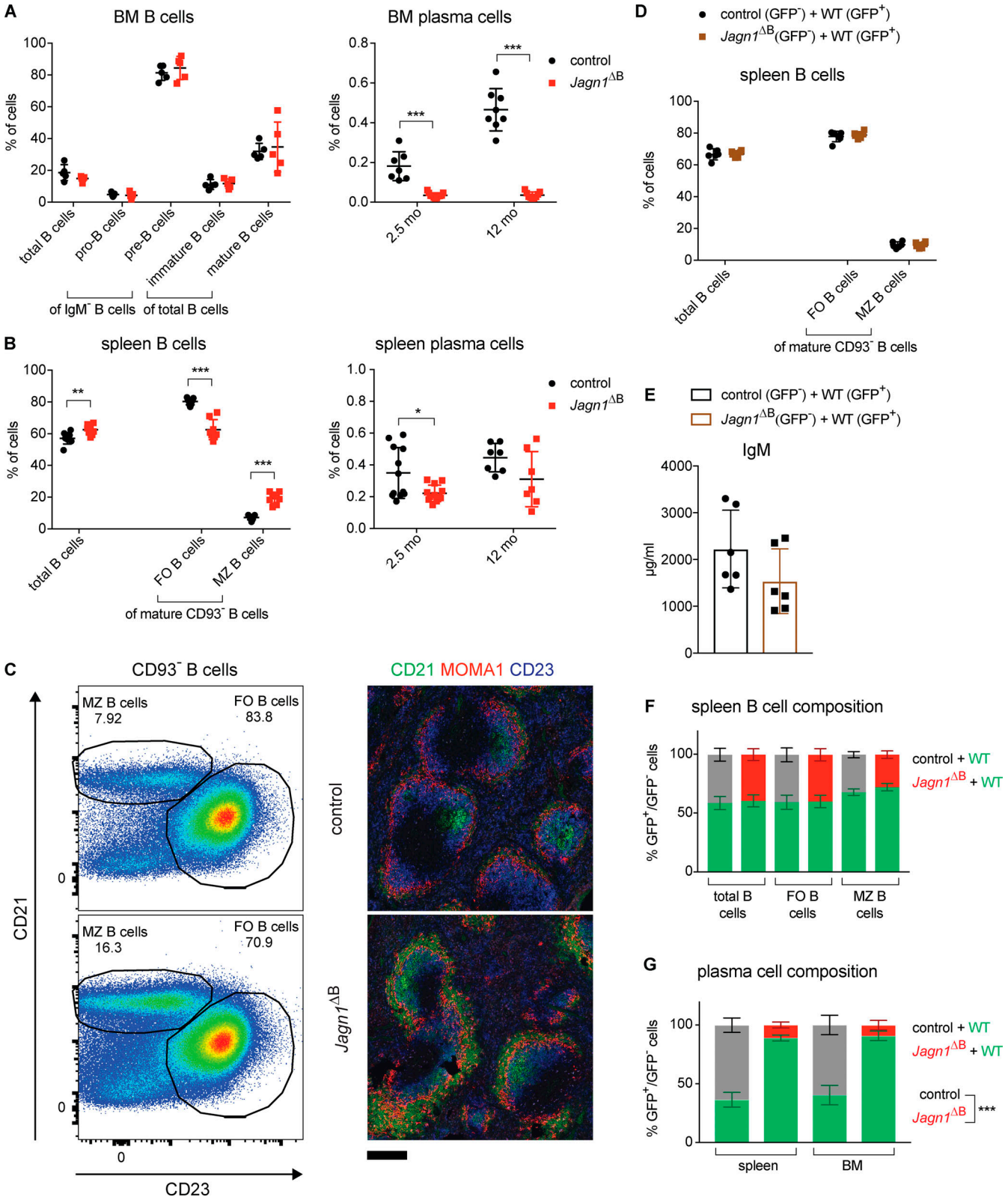

Figure 2. **Normal B cell development but altered splenic B cell homeostasis and reduced BM plasma cells in *Jagn1*$^{\Delta B}$ mice. (A)** Proportions of B cell developmental stages among BM CD19$^+$ B cells in 10-wk-old mice of the indicated genotypes (left panel; $n > 4$) and proportion of Lin$^-$CD138$^+$CD28$^+$ BM plasma cells in mice of the indicated ages and genotypes (right panel; $n > 6$). BM B cells included immature B cells (B220^{low}IgM$^+$), mature B cells (B220$^+$IgM$^+$), and precursor cells (IgM$^-$), which are divided into cKit$^+$ pro–B cells and CD2$^+$ pre–B cells, determined by flow cytometry. Lin$^-$ cells included all cells negative for the lineage markers TCRβ, CD23, CD11b, and CD49b. Data are shown for one of at least two independent experiments. **(B)** Percentages of total B cells and proportions of FO CD23$^+$CD21^{int} and MZ CD21$^+$CD23^{low} B cells among splenic mature CD19$^+$CD93$^-$ B cells in 10-wk-old mice of the indicated genotypes (left

panel; $n > 7$) and proportion of splenic Lin$^-$CD138$^+$CD28$^+$ plasma cells in mice of the indicated ages and genotypes (right panel; $n > 6$), as determined by flow cytometry. Data are shown for one of at least two independent experiments. **(C)** Representative flow cytometry staining for CD23 and CD21 on mature splenic CD19$^+$CD93$^-$ B cells of mice of the indicated genotypes (left panel). Right panels show splenic architecture as assessed by immunohistochemical staining for CD23, CD21, and the metallophilic macrophage marker MOMA1 to visualize splenic MZs (scale bar = 200 µm). In total, four mice per genotype were analyzed by immunohistochemistry. **(D)** Percentages of total B cells and proportions of splenic FO CD23$^+$CD21^{int} and MZ CD21$^+$CD23^{low} B cells among mature CD19$^+$CD93$^-$ B cells of mixed BM chimeric mice 4 mo after reconstitution, generated by reconstituting lethally irradiated mice with BM mixtures of the indicated genotypes at a 1:1 ratio ($n = 6$). Data are shown for one of two independent experiments. **(E)** IgM concentrations in sera from mixed BM chimeric mice, as described in D, assessed with an isotype-multiplexing assay ($n = 6$). Data are shown for one experiment. **(F)** Contribution of control and *Jagn1*$^{\Delta B}$ BM–derived cells to the indicated splenic B cell subsets in mixed BM chimeric mice, described in D, analyzed 4 mo after irradiation and BM reconstitution by flow cytometry ($n = 6$). Data are shown for one of two independent experiments. **(G)** Contribution of control and *Jagn1*$^{\Delta B}$ BM–derived cells to the indicated splenic and BM plasma cell populations in mixed BM chimeric mice 4 mo after irradiation and BM reconstitution, as assessed by flow cytometry ($n = 6$). Data are shown for one experiment. For panels A, B, D, and E, each data point represents an individual mouse. P values were calculated using the Student's *t* test and corrected for multiple comparisons using the Holm-Sidak method. The GFP-negative cells in panels F and G were analyzed by one-way ANOVA followed by Bonferroni correction. *, P < 0.05; **, P < 0.01; ***, P < 0.001. Error bars represent means ± SD.

Since *JAGN1* mutant patients exhibit phenotypic variability (Boztug et al., 2014), presumably caused by their differing genetic backgrounds, we next tested for mouse strain–specific effects on the observed B cell phenotypes. To this end, we crossed *Jagn1*$^{\Delta B}$ C57BL/6J mice onto C57BL/6J/129/Sv and C57BL/6J/BALB/c mixed backgrounds (Fig. S3 A). In all mixed backgrounds, *Jagn1*$^{\Delta B}$ mice showed a comparable phenotype of increased splenic MZ B cells, strongly decreased intracellular IgM levels in splenic and BM plasma cells, and markedly reduced numbers of long-lived BM plasma cells, whereas short-lived splenic plasma cells were apparently not affected by the loss of *Jagn1* (Fig. S3, B–D). Taken together, these data indicate that JAGN1 is cell-intrinsically required for the generation of plasma cells.

Increased ER stress and altered ER architecture in *Jagn1* mutant plasmablasts

To further analyze the consequences of *Jagn1* loss on antibody-secreting cells, we isolated splenic B cells from control and *Jagn1*$^{\Delta B}$ mice and stimulated them with LPS for 4 d to induce IgM secretion and plasma cell differentiation. LPS induces the sequential differentiation of naive B cells into activated B cells (CD22$^+$CD138$^-$), preplasmablasts (CD22^{low}CD138$^-$), and finally plasmablasts (CD22$^-$CD138$^+$; Minnich et al., 2016). LPS stimulation of *Jagn1*$^{\Delta B}$-derived B cells led to a significant albeit small reduction in antibody-producing preplasmablasts and plasmablasts (Fig. 3 A).

To study transcriptional changes in these in vitro–differentiated plasmablasts caused by *Jagn1* loss, we FACS sorted CD22$^-$CD138$^+$ plasmablasts and performed RNAseq, which revealed 521 (289 down and 232 up) differentially expressed genes (padj < 0.01; Fig. S4 A). Gene ontology (GO) enrichment analysis of the up-regulated genes revealed stress response, apoptosis, protein folding, unfolded protein response (UPR), or ER as overrepresented categories in *Jagn1*$^{\Delta B}$ plasmablasts (Fig. 3 B). The up-regulated UPR/stress-response genes included genes encoding chaperones (such as *Hspa1a*, *Hspa1b*, and *Hspa8*), transcriptional regulators (*Atf4*, *Atf5*, *Ddit3*, and *Nupr1*), and enzymes (*Fkbp11* and *Ppp1r15a*) and other known UPR target genes (*Gadd45a* and *Sqstm1*) to assist in protein folding and relieving ER stress. We therefore measured ER stress in *Jagn1*$^{\Delta B}$ plasmablasts compared with littermate control-derived cells. *Jagn1*-deficient plasmablasts indeed showed increased ER stress as evidenced by enhanced *X-box binding protein 1* (*Xbp1*) splicing (Fig. 3, C and D) and increased spliced XBP1 protein levels (Fig. 3 E). Furthermore, we found up-regulated Golgi stress genes including *Fut1* and *Golgb1*, which are involved in maintaining Golgi homeostasis (Serebrenik et al., 2018). To further assess whether *Jagn1* loss and the observed ER stress affects the Golgi apparatus, we stained cells with the Golgi Cytopainter dye to measure Golgi content by flow cytometry. We found a decreased Golgi Cytopainter fluorescence intensity in *Jagn1*$^{\Delta B}$ plasmablasts (Fig. S4 C), suggesting a reduced abundance of Golgi compartments. Additional evidence for an impact on the endomembrane system was an increase in the LysoTracker signal in *Jagn1*$^{\Delta B}$ plasmablasts, indicative of a higher abundance of acidic compartments (Fig. S4 D). Down-regulated GO categories in our RNA sequencing analysis included sterol and lipid synthesis as well as metabolism (Fig. S4 B). Since plasma cell differentiation requires an extensive increase in lipid metabolism for ER synthesis, we next tested for the impact of *Jagn1* deletion on the structure of the ER. JAGN1 inactivation was associated with a massively altered ER structure in plasmablasts as analyzed by electron microscopy (Fig. 3 F). Thus, loss of ER-localized JAGN1 in B cells leads to increased ER stress as well as marked changes in ER architecture in antibody-secreting plasmablasts.

Jagn1 deficiency results in diminished Ig production

To test for the ability of *Jagn1* KO B cells to produce Ig in response to LPS stimulation in vitro, intracellular and secreted IgM levels were quantified for *Jagn1*-deficient and -sufficient B cells. Loss of JAGN1 led to a substantial reduction in intracellular and secreted Ig when compared with Ig levels of control cells (Fig. 3, G and H; and Fig. S4, E and F). Of note, transcript levels for both membrane (µM) and secreted (µS) mRNA species were comparable in *Jagn1*-sufficient and -deficient cells (Fig. 3 I). Similar results were obtained in a more "physiological" in vitro differentiation system—the iGB culture—to generate germinal center–like class-switched B cells (Fig. 4 A). Control and *Jagn1*-deficient B cells were co-cultured on 40LB stromal cells expressing membrane-bound CD40L and producing the pro-survival B cell activating factor to support optimal proliferation of B cells. In addition, cells were stimulated with IL-4 for 4 d followed by 4 d of IL-21 stimulation to generate IgG1 and IgE class-switched plasmablasts (Nojima et al., 2011; Wöhner et al., 2016). Using this assay, *Jagn1*-deficient B cells generated an altered ratio of

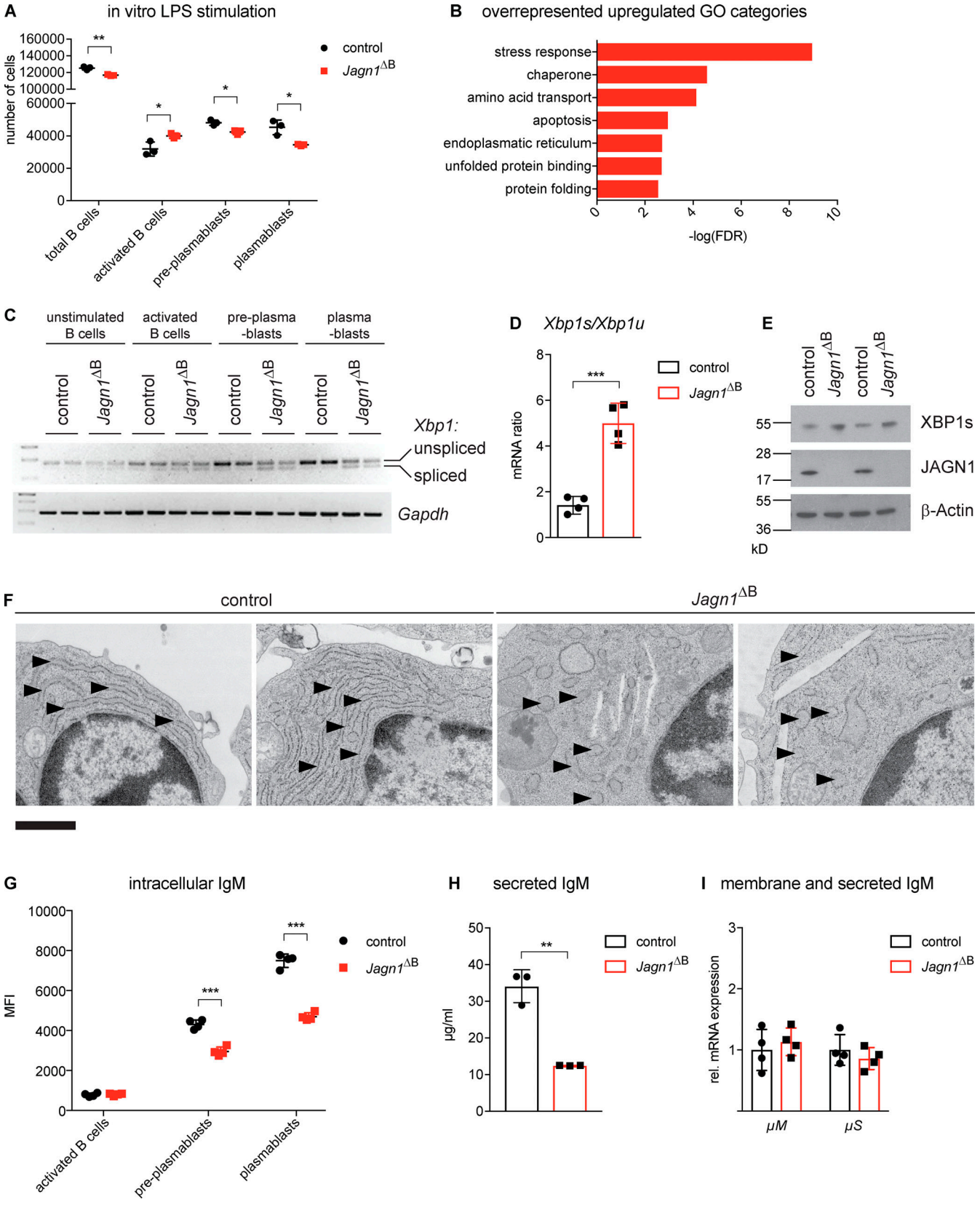

Figure 3. **Increased ER stress, altered ER structure, and reduced intracellular and secreted IgM in in vitro LPS-stimulated splenic B cells. (A)** Numbers of total B cells, activated B cells ($CD22^{+}CD138^{-}$), preplasmablasts ($CD22^{low}CD138^{-}$), and plasmablasts ($CD22^{-}CD138^{+}$) at day 4 of in vitro LPS stimulation of splenic B cells isolated from mice of the indicated genotypes analyzed by flow cytometry (n = 3). Data are shown for one of two independent experiments. **(B)** Top-enriched GO biological processes and keywords among up-regulated genes, as assessed by QuantSeq 3′ mRNA sequencing of mRNA derived from

Jagn1$^{\Delta B}$ versus control plasmablasts (n = 4) differentiated as in A and analyzed by DAVID GO analysis. GO terms are ranked by the negative logarithm of the false discovery rate (FDR; padj < 0.01). **(C)** Splicing of *Xbp1* mRNA in unstimulated B cells, or the indicated activated B cell subsets sorted from LPS-stimulated cultures (as described in A), assessed by semiquantitative RT-PCR analysis compared with the housekeeping gene *Gapdh*. Data are shown for one of three independent experiments. **(D)** Ratio of spliced (*s*) versus unspliced (*u*) *Xbp1* mRNA in sorted control and *Jagn1*$^{\Delta B}$ plasmablasts differentiated as described in A, assessed by qRT-PCR (n = 4). Data are shown for one of two independent experiments. **(E)** Immunoblot analysis to test for XBP1s (spliced XBP1) and JAGN1 protein levels in cell lysates from sorted plasmablasts of the indicated genotypes generated as described in A. β-Actin protein levels are shown as loading control. Data are shown for one of two independent experiments. **(F)** Representative electron micrographs of plasmablasts of the indicated genotypes generated as described in A. Arrowheads indicate the ER (scale bar = 1 µm). Images are representative for B cell cultures derived from four individual mice. **(G)** Intracellular IgM levels in the indicated B cell subsets generated as in A, assessed by intracellular staining and analysis by flow cytometry (n = 4). Graph depicts median fluorescence intensity (MFI). Data are shown for one of two independent experiments. **(H)** Secreted IgM concentrations in supernatants of cell cultures as described in A, determined by isotype-multiplexing assay (n = 3). Data are shown for one of two independent experiments. **(I)** Relative mRNA expression levels of membrane (*µM*) and secreted (*µS*) IgM in plasmablasts of the indicated genotypes sorted from cultures as described in A, analyzed by qRT-PCR (n = 4). *Gapdh* was used as housekeeping control, and the average of the control was set to 1. Data are shown for one of two independent experiments. For panels A, D, and G–I, each data point represents an individual mouse (or cells originating from an individual mouse). P values were calculated using the Student's *t* test and corrected for multiple comparisons using the Holm-Sidak method. *, P < 0.05; **, P < 0.01; ***, P < 0.001. Error bars represent means ± SD.

early activated B cells and preplasmablasts but the same number of plasmablasts when compared with control cells (Fig. 4 B). This is in accordance with our observation that splenic plasma cells were found at normal levels in *Jagn1*$^{\Delta B}$ mice (Fig. 2 B and Fig. S3 C). However, *Jagn1*$^{\Delta B}$ plasmablasts exhibited a substantial decrease in IgE and IgG1 production as shown by reduction in both spot numbers and sizes in ELISPOT assays (Fig. 4, C–E).

To analyze the contribution of cell death to the observed *Jagn1*$^{\Delta B}$ plasma cell phenotype, we crossed *Jagn1*$^{\Delta B}$ mice to *Vav-Bcl2* transgenic mice overexpressing the anti-apoptotic BCL-2 protein in the hematopoietic lineage (Ogilvy et al., 1999). Under conditions of severe and sustained ER stress, pro-apoptotic signals trigger the intrinsic apoptosis pathway by inhibiting anti-apoptotic BCL-2, leading to cytochrome C release from mitochondria, activation of caspases, and ultimately apoptotic cell death (Hetz and Papa, 2018; Urano et al., 2000; Tournier et al., 2000; Lei and Davis, 2003). Overexpression of BCL-2 resulted in reduced numbers of early apoptotic cells (Annexin V$^+$ propidium iodide [PI]$^-$) and late-apoptotic or dead cells (Annexin V$^+$PI$^+$), thereby strongly increasing the fraction of viable cells (Annexin V$^-$PI$^-$) after 4 d of LPS stimulation of control as well as *Jagn1*$^{\Delta B}$ splenic B cells in vitro (Fig. 4 F). Importantly, overexpression of BCL-2 substantially increased the number and proportion of BM plasma cells in control mice, but only moderately in *Jagn1*$^{\Delta B}$ mice (Fig. 4 G). Overexpression of BCL-2 could also not rescue the decreased serum IgM levels in vivo or intracellular IgM levels of plasmablasts generated by LPS stimulation of *Jagn1*-deficient splenic B cells (Fig. 4 G). This might be explained by the fact that continuous ER stress leads to an apoptotic signal that at one point overexpression of anti-apoptotic BCL-2 cannot overcome. These data indicate that while the reduced number of plasma cells observed in *Jagn1*$^{\Delta B}$ mice as compared with non-*Bcl2* transgenic mice can be partially rescued, enhancing cell survival does not restore the impaired IgM levels of *Jagn1*$^{\Delta B}$ antibody-producing cells.

Loss of JAGN1 in B cells leads to altered glycosylation of Ig

Serum IgG comprises multiple glycoforms as a result of the addition of complex N-glycans to the IgG Fc domain during trafficking through the ER and Golgi (Takahashi et al., 1987; Raju et al., 2000). IgG glycoform profiles have been reported to vary with age, genetic background, sex, pregnancy, and disease states (de Haan et al., 2016; Pucić et al., 2011; Bondt et al., 2013; Seeling et al., 2017; Zhang et al., 2016; Ackerman et al., 2013). However, the specific endogenous mechanisms that control distinct Ig glycosylation patterns in plasma cells are poorly understood. Typically, IgG-attached glycans are di-antennary, complex-type, N-linked glycans, including combinatorial variants of the common fucosylated N-glycan core structure (i.e., two N-acetylglucosamine residues [GlcNAc] extended by a central mannose and two distal branching mannoses) and its extensions by one additional GlcNAc residue on each mannose, followed by one galactose and terminated by one sialic acid residue (Fig. 5 A).

Considering the fact that *Jagn1* mutant neutrophils exhibited aberrant N-glycosylation of multiple neutrophil effector proteins in mice and humans (Wirnsberger et al., 2014; Boztug et al., 2014), we speculated that this role of JAGN1 is not limited to neutrophils but that JAGN1 might also be involved in antibody glycosylation. To investigate this hypothesis, we assessed the relative abundance of IgG subclass–specific glycopeptide glycoforms purified from mouse serum by liquid chromatography electrospray ionization mass spectrometry (LC-ESI-MS). IgG peptides from *Jagn1*$^{\Delta B}$ mice exhibited altered glycoprofiles defined by reduced fucosylation (GnGnF) of IgG2 and IgG3 as well as increased galactosylation (AA) of IgG3 and sialylation (NgAF and NgNgF) of IgG2 and IgG3 when compared with Ig from their control littermates (Fig. 5 B). Additionally, sera of *Jagn1*$^{\Delta B}$ mice contained nonfucosylated GnGn and AGn glycoforms, which were absent in control littermates. The strongest difference was found in fucosylated GnGnF IgG3 (28.22% in control vs. 13.78% in *Jagn1*$^{\Delta B}$ mice; Fig. 5 B).

The observed differences in antibody glycosylation could be due to a direct effect of *Jagn1* deficiency on the glycosylation machinery or due to the increased ER stress and thereby decreased antibody glycosylation and secretion in *Jagn1*-deficient plasma cells. To explore these mutually nonexclusive hypotheses, we analyzed mice lacking the ER stress sensor inositol-requiring enzyme 1 (IRE1) in the hematopoietic lineage using *Vav1*-Cre as a deleter line (*Ire1*$^{\Delta hem}$). IRE1 is an essential component of the UPR pathway important for sensing and responding to ER stress by splicing of its downstream transcription factor *Xbp1* (Bettigole et al., 2015) and has been reported to be required for efficient B cell differentiation (Zhang et al., 2005). In plasma cells, IRE1/XBP1 is not required for

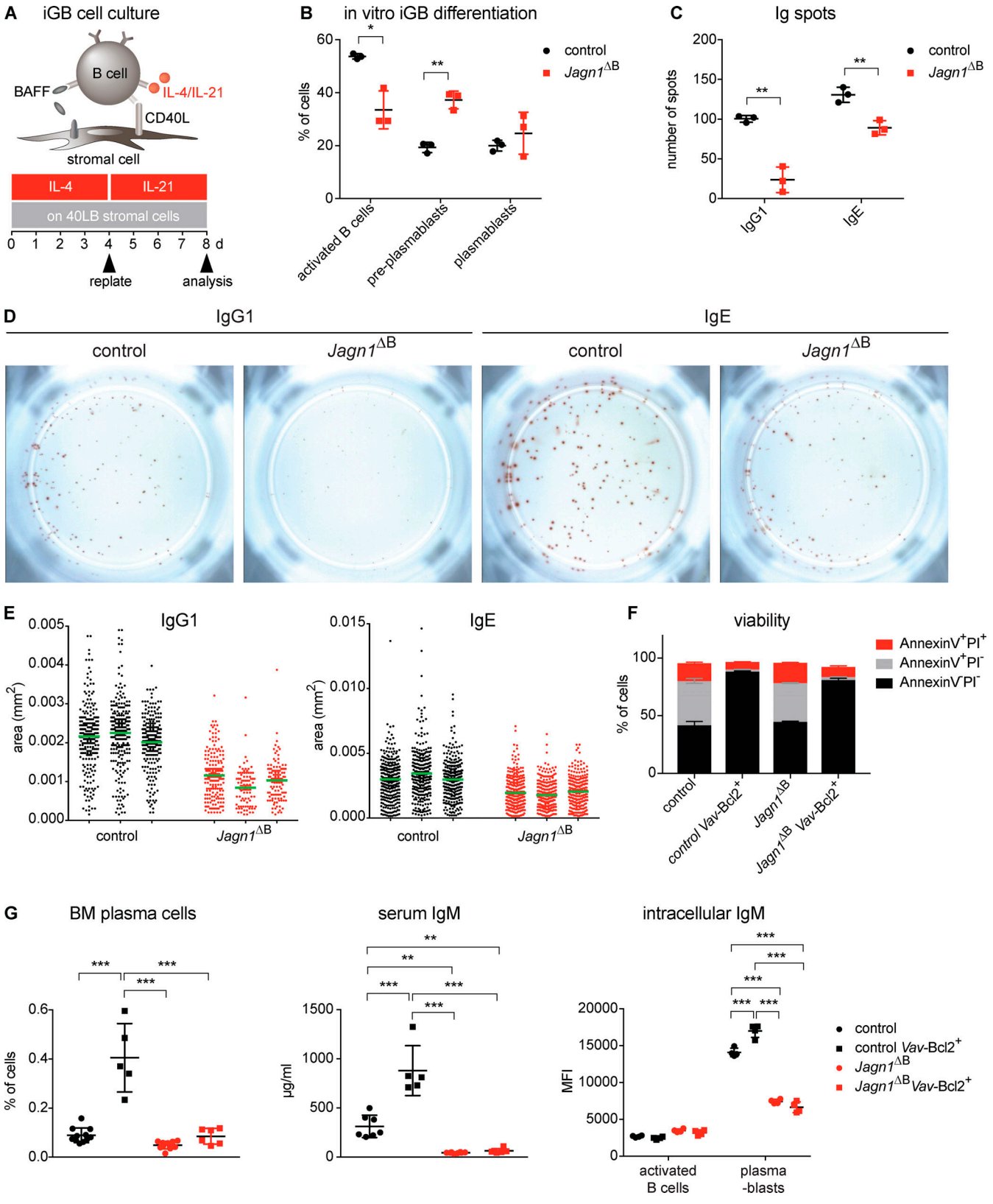

Figure 4. **Increasing the survival of antibody-producing cells does not restore Ig production in *Jagn1*$^{\Delta B}$ mice. (A)** Schematic representation of the iGB cell culture system for in vitro plasmablast differentiation: stromal 40LB cells express membrane-bound CD40L and produce the pro-survival B cell activating factor (BAFF) to support optimal proliferation of B cells in the presence of IL-4 and subsequently IL-21. **(B)** B cell numbers of activated B cells ($CD23^+CD138^-$), preplasmablasts ($CD23^{low}CD138^-$), and plasmablasts ($CD23^-CD138^+$) from iGB cultures of B cells of the indicated genotypes at day 8 of differentiation (n = 3). Data are shown for one of two independent experiments. **(C)** Numbers of IgG1- and IgE-secreting cells differentiated in iGB cultures as

assessed by ELISPOT analysis at day 8 of differentiation. For the analysis, 200 control and *Jagn1*$^{\Delta B}$ CD19$^+$CD138$^+$IgG1$^+$ or CD19$^+$CD138$^+$IgE$^+$ cells were sorted in duplicates on ELISPOT plates coated with anti-IgG1/IgE, respectively. Duplicates were averaged and each data point represents cells of an individual mouse (n = 3). Data are shown for one of two independent experiments. **(D)** Representative images of IgG1 (left panel) and IgE (right panel) ELISPOT assay plates for sorted control and *Jagn1*$^{\Delta B}$ cells. **(E)** Quantification of spot sizes of IgG1- or IgE-secreting cells from ELISPOT analysis of cultures as described in A for cells from three individual mice. Green lines indicate mean spot sizes. Data are shown for one of two independent experiments. **(F)** Proportions of viable (Annexin V$^-$PI$^-$), early-apoptotic (Annexin V$^+$PI$^-$), and late-apoptotic/dead cells (Annexin V$^+$PI$^+$) as determined by flow cytometry after 4 d of LPS stimulation of control, control *Vav*-Bcl2$^+$, *Jagn1*$^{\Delta B}$, and *Jagn1*$^{\Delta B}$ *Vav*-Bcl2$^+$ splenic B cells (n = 2). Data are shown for one of two independent experiments. **(G)** Proportions of Lin$^-$CD138$^+$CD28$^+$ BM plasma cells (left panel; n > 4; data from two independent experiments are pooled) and IgM serum concentrations (middle panel; n > 4; data from two independent experiments are pooled) in mice of the indicated genotypes. The right panel depicts the median fluorescence intensity (MFI) of intracellular IgM expression levels in activated B cells (CD22$^+$CD138$^-$) and plasmablasts (CD22$^-$CD138$^+$) after 4 d of LPS stimulation in vitro, as assessed by intracellular staining and flow cytometry (data are shown for one of two independent experiments). For panels B, C, and G, each data point represents an individual mouse (or cells originating from an individual mouse). P values were calculated using the Student's t test and corrected for multiple comparisons using the Holm-Sidak method, with the exception of those in G (one-way ANOVA followed by Bonferroni correction). *, P < 0.05; **, P < 0.01; ***, P < 0.001. Error bars represent means ± SD.

differentiation, but to increase the secretory apparatus for Ig synthesis (Taubenheim et al., 2012). When we assayed *Ire1*$^{\Delta hem}$ mice, we observed markedly reduced serum Ig levels (Fig. S4 G), very similar to *Jagn1*$^{\Delta B}$ mice. Importantly, the antibody glycosylation changes we had observed in *Jagn1*$^{\Delta B}$ mice were also found in sera of *Ire1*$^{\Delta hem}$ mice (Fig. 5 C). Together, these data reveal an important role for the ER stress response in the altered glycoprofile of serum Ig in *Jagn1*$^{\Delta B}$ mice.

Altered biological properties of *Jagn1*$^{\Delta B}$ Ig

Reduced IgG fucosylation and increased sialylation, as observed in *Jagn1*$^{\Delta B}$ Ig, have been shown to strengthen IgG binding to Fcγ receptors (Shields et al., 2002; Lin et al., 2015; Shinkawa et al., 2003; Okazaki et al., 2004; Ferrara et al., 2011), thereby leading to altered effector functions. Analyses of *Rag2*$^{-/-}$ mice transfused with serum of control or *Jagn1*$^{\Delta B}$ mice (normalized to equal amounts of IgG) showed no change in Ig stability (Fig. S5 A). Furthermore, the respective Fc-glycosylation profiles remained stable over the time of analysis (Fig. S5 B). However, incubation of BM cells isolated from *Rag2*$^{-/-}$ mice with serum of *Jagn1*$^{\Delta B}$ mice yielded an increased fraction of surface-bound IgG on neutrophils, indicating enhanced IgG binding to Fcγ receptors (Fig. 5 D). The augmented binding of serum IgG from *Jagn1*$^{\Delta B}$ mice to CD11b$^+$Ly6G$^+$ neutrophils was not observed for CD11b$^+$Ly6G$^-$ myeloid cells and was strongly diminished by blocking the Fcγ receptors with CD16/32 antibodies, indicating Fc receptor–specific binding (Fig. 5 E). Notably, *Jagn1*$^{\Delta B}$ mice exhibited an increased fraction of Fc receptor–bound IgG on isolated BM neutrophils despite the fact that these animals had severely reduced total IgG serum levels compared with littermate control mice (Fig. 5 F). To assess whether the increased Fc receptor binding of *Jagn1*$^{\Delta B}$ IgG has functional consequences, we performed neutrophil-mediated ADCC assays with E0771 breast cancer cells. E0771 cells were opsonized with control and *Jagn1*$^{\Delta B}$ Ig from E0771 tumor–bearing mice, resulting in antibody coating of the E0771 cells (Fig. S5, C and D). *Jagn1*$^{\Delta B}$ sera or purified IgG resulted in a higher percentage of dead tumor cells than their wild-type counterparts when mixed with increasing E/T ratios of *Rag2*-deficient BM cells (Fig. 5 G) or purified neutrophils (Fig. 5 H). These data indicate that the enhanced Fc receptor binding results in increased ADCC by neutrophils toward cancer cells coated with *Jagn1*$^{\Delta B}$ IgG.

Interestingly, after Ig purification of *Jagn1*$^{\Delta B}$ sera with protein G beads, additional bands were visible on Coomassie-stained protein gels despite the overall reduction of Ig levels (Fig. S5 E). Using tandem MS, these bands were identified as complement protein C3, a central component of the complement system. Immunoblotting for complement C3 revealed no difference in total C3 complement levels between control and *Jagn1*$^{\Delta B}$ mouse sera (Fig. S5 F), but after Ig purification by protein G we observed increased binding of complement protein C3 to *Jagn1*$^{\Delta B}$ mouse serum–derived Ig (Fig. S5 G). Together, this indicates that the glycosylation changes in *Jagn1*$^{\Delta B}$-derived IgG enhance their binding to Fcγ receptors and complement components.

JAGN1 rare disease mutations affect the Ig glycoprofile in humans

Mutations in the human *JAGN1* gene cause severe congenital neutropenia (Boztug et al., 2014), and a recent report showed that some *JAGN1* patients also suffer from hypogammaglobulinemia (Baris et al., 2015). We therefore analyzed sera from patients with homozygous missense mutations (P6: c.59G>A; p.Arg20Glu, P9: c.40G>A; p.Gly14Ser, P12: c.63G>T; p.Glu21Asp) or a nonframeshift deletion mutation in *JAGN1* (P14: c.3543del CCGACGGCA; p.Thr12Gly14del) leading to expression of a mutant and likely nonfunctional protein (Boztug et al., 2014). Importantly, even though the serum Ig levels were within normal limits, we detected an altered Ig glycoprofile of the most abundant IgG1 subclass in sera from patients carrying *JAGN1* mutations when compared with healthy donors (Fig. 6 A). Moreover, in patient-derived Epstein-Barr virus–transformed B lymphoblastoid cells, we detected increased signs of ER stress including elevated *XBP1* splicing and up-regulation of *heat shock protein family A member 5* (*HSPA5*; Fig. 6 B). These data show that loss of functional JAGN1 protein in congenital neutropenia patients is associated with changes in Ig N-glycosylation and alterations in ER homeostasis and function in B cells, resembling the described phenotypes observed in our *Jagn1*$^{\Delta B}$ mouse model.

Discussion

In this study, we identify a crucial role for the ER protein JAGN1 in humoral immunity. Deletion of *Jagn1* in B cells led to defects in the differentiation and maintenance of long-lived BM plasma cells by causing increased ER stress and decreased antibody production and secretion, as well as marked alterations in the N-glycosylation of Ig. Consequently, *Jagn1*$^{\Delta B}$ mice exhibited

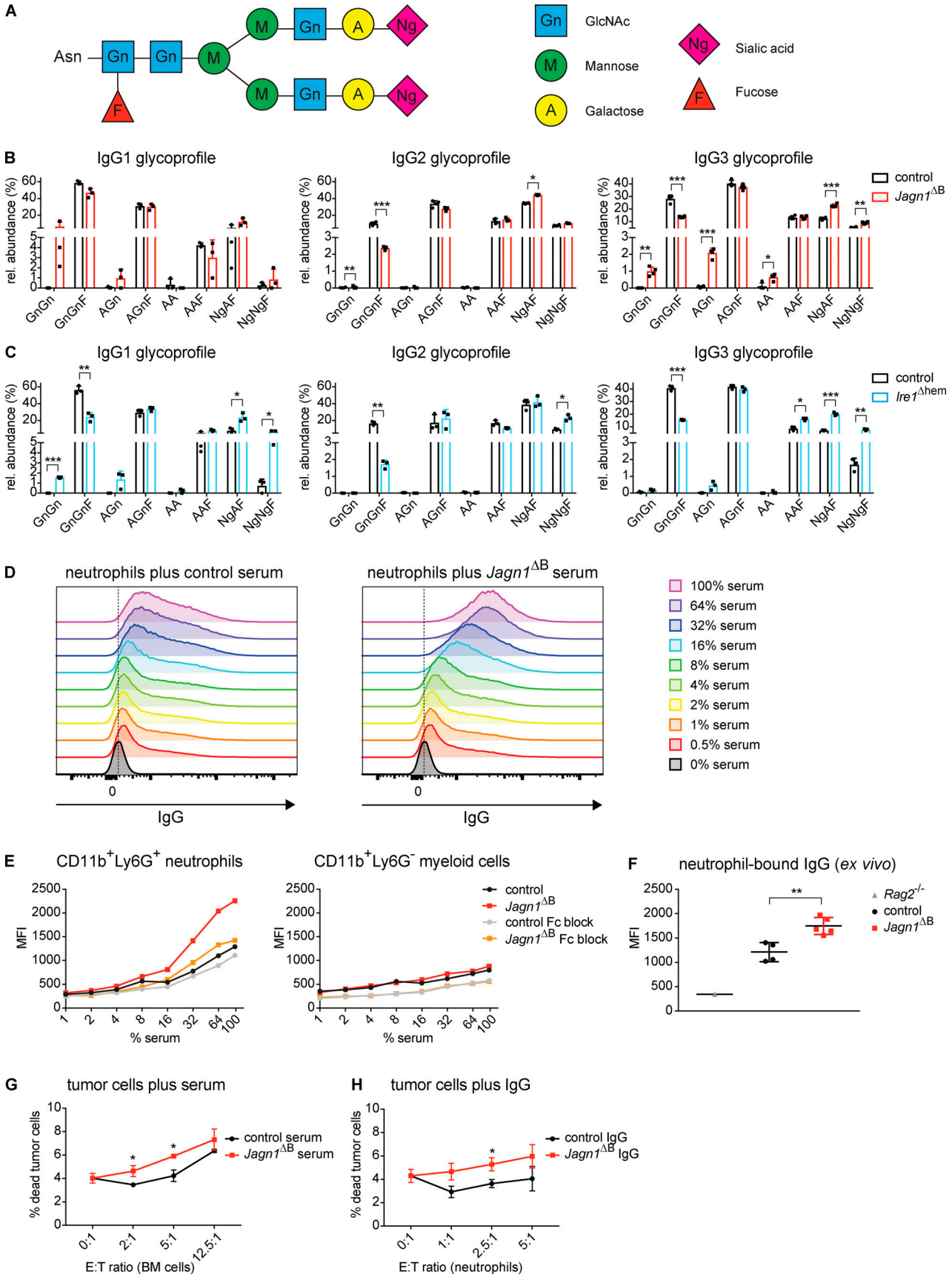

Figure 5. **Altered Ig glycoprofile and increased Fc receptor binding of Ig in *Jagn1*$^{\Delta B}$ mice. (A)** Schematic representation of a glycan tree attached to IgG heavy chain Asn297. The glycan tree contains monomers of N-acetylglucosamine (Gn, GlcNAc), fucose (F), mannose (M), galactose (A), and sialic acid (Ng).

(B and C) Relative abundance of serum IgG1, IgG2, and IgG3 glycoforms from control and *Jagn1*$^{\Delta B}$ mice (n = 3; B) and from control and *Ire1*$^{\Delta hem}$ mice (n = 3; C), as assessed by LC-ESI-MS. IgG3 glycoforms are abbreviated according to the ProGlycan nomenclature denoting the terminal residues of the two chains. Data are shown for one of four (B) and two (C) independent experiments. **(D)** Histograms depict analyses of neutrophil Fc receptor binding of serum IgG isolated from mouse sera. BM neutrophils (Ly6G$^+$) were isolated from *Rag2*-deficient mice and incubated with decreasing amounts of sera from mice of the indicated genotypes. Fc receptor–bound IgG was assessed by cell surface staining for IgG using flow cytometry. Data are shown for one of three independent experiments. **(E)** Binding of serum IgG to BM CD11b$^+$Ly6G$^+$ neutrophils (left panel) and CD11b$^+$Ly6G$^-$ myeloid cells (right panel) isolated from a *Rag2*$^{-/-}$ mouse in the presence or absence of an Fc receptor–blocking antibody (anti-CD16/32). Mean fluorescence intensity (MFI) of surface IgG staining is shown for increasing concentrations of serum antibodies from *Jagn1*$^{\Delta B}$ mice. Data are shown for one of two independent experiments. **(F)** Mean fluorescence intensities (MFI) of IgG bound ex vivo to neutrophils isolated from the BM of mice of the indicated genotypes (n > 3). Neutrophils isolated from a *Rag2*-deficient mouse that lacks B cells and Ig are shown as negative control. Data are shown for one of three independent experiments. **(G and H)** E0771 target cell killing as assessed by viability staining and flow cytometry of E0771 cancer cells after incubation with control and *Jagn1*$^{\Delta B}$ sera (G) or purified IgG (H) from E0771 tumor–bearing mice and addition of denoted E/T ratios (n = 3). Effector cells were *Rag2*-deficient BM cells containing ∼50% neutrophils (G) or freshly isolated Ly6G-enriched BM neutrophils (H). Data are shown for one of two (G) and three (H) independent experiments. For panels B, C, and F, each data point represents an individual mouse. P values were calculated using the Student's t test and corrected for multiple comparisons using the Holm-Sidak method. *, P < 0.05; **, P < 0.01; ***, P < 0.001. Error bars represent means ± SD.

reduced serum Ig levels at steady state and failed to mount an efficient humoral immune response upon infection with VSV or decreased antibody titers upon immunization with model antigens when compared with littermate control animals. Serum antibodies of *Jagn1*$^{\Delta B}$ mice displayed alterations in complement and Fc receptor binding, indicative of the functional relevance of their altered antibody glycosylation. Importantly, antibody glycosylation changes and increased ER stress in B cells observed in this mouse model were also detected in human patients carrying *JAGN1* mutations, highlighting the relevance of these findings for basic B cell biology and extending our understanding of the observed human rare-disease phenotype.

JAGN1 mutations have been described to alter ER function in the process of neutrophil granule formation and the glycosylation of neutrophil effector molecules (Boztug et al., 2014). We therefore hypothesized that JAGN1 might also affect B cells, which require extensive ER remodeling as an adaptation to produce and secrete massive amounts of glycosylated antibodies (Hibi and Dosch, 1986). Our data show that loss of JAGN1 in B cells results in profound alterations in Ig glycosylation. The complex carbohydrate structures linked to Asn297 of IgG do not affect antigen binding but rather modulate downstream effector functions by altering the conformation and biological properties of the Fc region, which acts as the prime interaction interface between the adaptive and innate immune system (Woof and Burton, 2004). Following Fc binding to Fc receptors on innate immune cells, nonclassical Fc receptors, and complement proteins, activation of these receptors can drive ADCC, CDC, phagocytosis, or neutrophil activation, all of

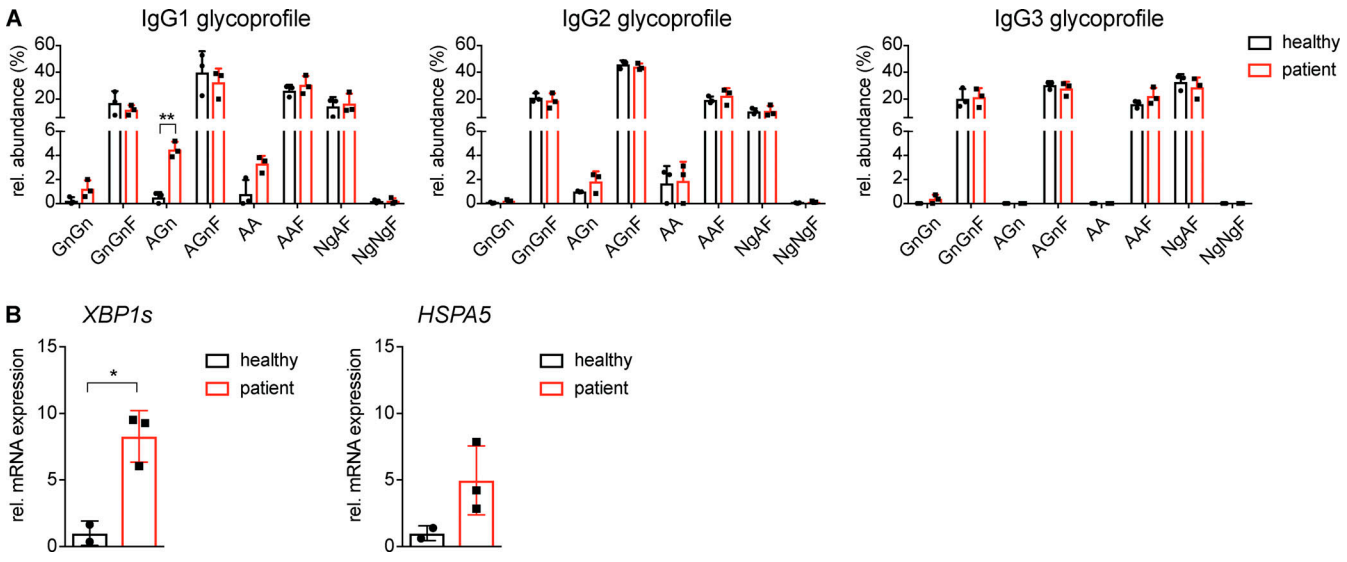

Figure 6. **Altered serum Ig glycoprofile in *JAGN1* mutant patients and increased ER stress in patient-derived B cell lines. (A)** Relative abundance of IgG1, IgG2, and IgG3 glycoforms on Asn297 in sera of healthy individuals and three *JAGN1* mutant patients (patients P6, P9, and P12 described in Boztug et al., 2014), as assessed by LC-ESI-MS (n = 3). IgG1 glycoforms are abbreviated according to the ProGlycan nomenclature denoting the terminal residues of the two chains. Data are shown for one of two independent experiments. **(B)** Relative mRNA expression levels of spliced *XBP1* (*XBP1s*; left) and *HSPA5* (right) in Epstein-Barr virus–transformed lymphoblastoid cell lines derived from healthy individuals (n = 2) or three *JAGN1* mutant patients (P6, P12, and P14 from Boztug et al., 2014). Values were normalized to the expression of the housekeeping gene *ACTB*, and the average of the healthy controls was set to 1. Data are shown for one of two independent experiments. For panels A and B, each data point represents a serum sample (A) or cells (B) originating from an individual healthy donor or patient. P values were calculated using the Student's t test and corrected for multiple comparisons using the Holm-Sidak method. *, P < 0.05; **, P < 0.01. Error bars represent means ± SD.

which are severely compromised for nonglycosylated IgG (Jefferis, 2009). Our data now identify the ER protein JAGN1 as a novel and critical regulator of antibody glycosylation.

The B cell phenotypes observed in our study regarding Ig levels are reminiscent of genetic impairment of the UPR in *Ire1*-deficient B cells. We now also found altered N-glycosylation of IgG secreted by *Ire1* mutant B cells. The concept that inhibiting N-glycosylation causes an accumulation of mis- or unfolded glycoproteins, thereby leading to ER stress, was established a long time ago (Zinszner et al., 1998; Koizumi et al., 1999; Brewer et al., 1999; Caspersen et al., 2000). Here, for the first time, we provide evidence that this crosstalk is bidirectional, where increased ER stress can also lead to altered N-glycosylation. It is therefore tempting to speculate that the Ig of *Jagn1*$^{\Delta B}$ mice or antibodies generated during increased ER stress (as observed in *Ire1*$^{\Delta hem}$ mice) might alter their effector functions and lead to increased ADCC and CDC. Glycosylation changes under elevated ER stress might be a regulatory mechanism used, for instance, during severe infections. To relieve ER stress, IRE1 oligomerizes and thereby autoactivates its RNase domain and splices *Xbp1* (Yoshida et al., 2001). The spliced *Xbp1* (*Xbp1s*) mRNA encodes a functional transcription factor, which regulates a variety of genes encoding chaperones and enzymes involved in protein folding and lipid synthesis (Lee et al., 2003; Sriburi et al., 2004; McGehee et al., 2009), thereby contributing to the ER expansion and increased Ig production in plasma cells. Of note, deficiency of *Jagn1* has more severe phenotypic consequences than deletion of *Xbp1*, which leads to a reduced density and organization of the ER as well as decreased antibody secretion, but not to a reduction in antibody-secreting cells (Taubenheim et al., 2012). Interestingly, we found that loss of *Jagn1* does not only result in increased ER stress, but also affects the Golgi apparatus, where IgG fucosylation and sialylation occur. This is in accordance with a previous study showing that JAGN1 interacts with members of the coat protein complex I, which plays an important role in vesicular trafficking between Golgi and ER (Boztug et al., 2014), which might explain the observed N-glycosylation changes.

Technological advances, especially in DNA sequencing, have vastly increased our understanding of the genetic basis of thousands of monogenic disorders. Mutations in *JAGN1* have been identified to be causative for severe congenital neutropenia by affecting the differentiation and survival of mature neutrophils (Boztug et al., 2014). Importantly, mutations in *JAGN1* are associated with considerable phenotypic variance. Additionally, defects in humoral immunity have been described for some patients (Baris et al., 2015). This phenotypic variability in genetic disorders could be a consequence of both differences in disease-causing mutations and genetic backgrounds as well as exposure to different pathogens. Indeed, differences in genetic backgrounds have been shown to compensate for deleterious genetic defects in human patients (Chen et al., 2016). Further increasing the complexity of genetic disorders of the immune system is the concerted contribution of different cell types to immune responses. Disentangling cause from consequence is therefore often difficult. In this study, we address these challenges by generating a model allowing us to decipher the phenotypic consequences of *Jagn1* mutations in humoral immunity. Importantly, phenotypic defects in humoral immunity—altered antibody glycosylation and increased ER stress in B cells—were observed both in our murine model system as well as in human rare-disease patients. Our data uncover a novel path required for effective antibody-mediated immunity.

Materials and methods

Mice

Jagn1fl/fl (Jagn1tm1c(EUCOMM)Hmgu), Ire1fl/fl (Ern1tm1Tiw), Mb1-Cre (Cd79atm1(cre)Reth), Cd23-Cre (Tg(Fcer2a-cre)5Mbu9), Vav1-Cre (Tg(Vav1-cre)A2Kio/J), Blimp1-GFP (Prdm1tm1Nutt), and Vav-Bcl2 (Tg(VavBCL2)1Jad) mice have been described previously and were bred on a C57BL/6 genetic background (Wirnsberger et al., 2014; Bettigole et al., 2015; Hobeika et al., 2006; Kwon et al., 2008; Kallies et al., 2004; Ogilvy et al., 1999). Rosa26-EGFP mice were generated by insertion of the gene encoding EGFP into the ubiquitously expressed *Rosa26* locus. Mouse genotypes were assessed by PCR (see Table S1 for genotyping primer sequences). Of note, only age- and sex-matched littermates from respective crosses were used for experiments. If not explicitly stated, experiments were performed 10–14 wk after birth. All mice were bred and maintained in accordance with ethical animal license protocols of the respective legal authorities. All animal experiments were approved by the Austrian Federal Ministry of Education, Science, and Research.

Isotyping and isotype-specific glycosylation analysis of serum antibodies

For antibody analyses, serum was prepared using serum-separating tubes (BD Biosciences) according to the manufacturer's instructions. IgG2b, IgG2c, IgG3, IgA, IgE, and IgM serum antibody titers were quantified using the Luminex xMAP technology-based Antibody Isotyping 7-Plex Mouse ProcartaPlex Panel 2 (ThermoFisher Scientific) according to the manufacturer's instructions. IgG1 serum antibody titers were determined by ELISA by using plates coated with anti-mouse IgG1. Mouse IgG1 antibodies were used in defined concentrations as control standards. For glycosylation analyses, ~1 µg of human or murine serum IgG was purified using protein G Dynabeads (ThermoFisher Scientific) and separated by SDS-PAGE. The Coomassie-stained SDS-PAGE bands representing the IgG heavy chain polypeptides were excised, destained, reduced, alkylated, and in-gel digested with trypsin (Trypsin Gold sequencing grade; Promega) as described previously (Stadlmann et al., 2008, 2009; Maresch and Altmann, 2016). Tryptic peptides and glycopeptides were separated by reversed-phase nano-HPLC (Acclaim PepMap C18, 75 µm × 50 cm; ThermoFisher Scientific) and analyzed by ESI-MS/MS (Q Exactive Hybrid Quadrupole-Orbitrap; ThermoFisher Scientific). The relative abundances of IgG subclass–specific glycopeptide glycoforms (Maresch and Altmann, 2016) were calculated from the manual integration (FreeStyle 1.3; ThermoFisher Scientific) of the respective extracted ion chromatographs.

Immunization and ELISPOT analyses

Mice were immunized intraperitoneally with 100 µg OVA (Sigma) adsorbed to 200 µl of alum as adjuvant. OVA-specific serum Ig titers were determined by ELISA of serial serum dilutions using 96-well plates (Maxisorp; Nunc) coated with 50 µg/ml OVA. Titers were determined using alkaline phosphatase–linked anti-IgG and anti-IgM detection antibodies (SouthernBiotech). Humoral responses to a T cell–dependent antigen were studied by intraperitoneal injection of 100 µg of 4-hydroxy-3-nitrophenylacetyl–conjugated KLH (NP-KLH)/alum. The frequencies of antibody-secreting cells in the spleen were determined by ELISPOT assays as described previously (Smith et al., 1997). Briefly, NP23-bio–coated plates were used for capturing antibodies secreted by individual cells. Spots were visualized with goat anti-mouse IgM or IgG antibodies conjugated to alkaline phosphatase (Southern Biotechnology Associates), and color was developed by the addition of BCIP/NBT Plus solution (Southern Biotechnology Associates). After extensive washing, spots were counted with an AID ELISPOT reader system (Autoimmun Diagnostika). The same procedure was used for the in vitro–cultured iGB cells, for which the ELISPOT plates were coated with anti-mouse IgE or IgG1 antibodies. 200 cells were sorted directly on the plates, which were either $CD19^+CD138^+IgG1^+$ or $CD19^+CD138^+IgE^+$, and were then incubated for 6 h. The area of the ELISPOTs was determined using the Fiji software ImageJ (version 2.0.0-rc65/1.51s).

VSV infections

Mice were infected with 2×10^6 PFU of VSV-containing full-length OVA (seed stock) via tail vein injection (Turner et al., 2008). Mice were bled at 3, 7, and 10 d after infection, and blood samples were centrifuged at 10,000 *g* for 5 min to collect serum. VSV-neutralizing antibodies in the serum were measured using a VSV neutralization assay. Briefly, 5 µl of serum was left untreated for total Ig or mixed with 5 µl of 0.1 M 2-mercaptoethanol for 1 h for IgG measurement (all complex isoforms were reduced and disassembled under this condition), subsequently diluted 1:40 in MEM containing 2% fetal calf serum, and heat inactivated for 30 min at 56°C. Twofold serial dilutions of serum samples were then mixed with 500 PFU/ml VSV, incubated for 90 min, and then added to monolayers of Vero cells. The cells were infected for 60 min in an incubator at 37°C and 5% CO_2 and then overlaid with methylcellulose and incubated for 24 h at 37°C and 5% CO_2. Subsequently, cells were stained with crystal violet stain, and titers were scored by the highest serum dilution, reducing the plaque numbers by 50% ($-\log_2 x40$).

Generation of mixed-BM chimeric mice

To generate BM chimeric mice, 8-wk-old *Rag2*-deficient mice were split dose irradiated (2 × 5.5 Gy) and reconstituted 18 h after the second irradiation with mixtures of B cell/T cell/NK cell–depleted donor cells using magnetic cell separation (MACS; Miltenyi Biotec; two million *Rosa*-EGFP and two million control/$Jagn1^{\Delta B}$ lineage–depleted donor cells per mouse) by intravenous injection. Experiments were performed 4 mo after reconstitution.

Flow cytometry

Antibody labeling of cells after ammonium-chloride-potassium lysis of red blood cells was performed in FACS buffer (PBS supplemented with 2% fetal calf serum and 2 mM EDTA) on ice for 30 min after blocking Fc receptors with CD16/CD32 Fc block (2.4G2; eBioscience) for 5 min to inhibit unspecific antibody binding. Cell viability was assessed with the Fixable Viability Dye eFluor780 (eBioscience). See Table S2 for a list of antibodies (BD Biosciences, Biolegend, or eBioscience) used in this study for flow cytometric analysis. Intracellular staining for JAGN1, IgM, and BLIMP1 was performed using the Foxp3 staining kit (eBioscience) according to the manufacturer's instructions. Cells were recorded on an LSR II flow cytometer (BD Biosciences), and data were analyzed using FlowJo v10.0.6 software (Tree Star). For viability analysis, cells were stained with Annexin V-BV605 (BD Biosciences) and PI (eBioScience) in Annexin V binding buffer (BD Biosciences) according to the manufacturer's instructions. For labeling of lysosomes, living cells were incubated in medium containing 50 nM LysoTracker Deep Red (ThermoFisher Scientific) for 30 min at 37°C, washed, stained with additional antibodies to distinguish the different cell populations, and immediately recorded using flow cytometry. For labeling of the Golgi apparatus, living cells were labeled with the Golgi/ER staining kit Cytopainter (Abcam) according to the manufacturer's instructions, stained with additional antibodies to distinguish the different cell populations, and immediately recorded using flow cytometry.

Immunofluorescence and immunohistochemistry

We performed a knockdown of endogenous *Jagn1* in the IgG2b-producing mouse B lymphocyte plasmacytoma cell line MPC-11 (ATCC CCL-167; BALB/c background). Additional expression of full-length JAGN1 fused to an amino-terminal V5 tag allowed immunofluorescence detection of V5-tagged JAGN1 in these cells. Transfected MPC-11 cells were washed in HBSS and stained with ER-Tracker Green (ThermoFisher Scientific; GenBank accession no. E34251, 1:3,000 in HBSS) for 30 min at 37°C. Following washing, cells were seeded on poly-D-lysine–coated coverslips and fixed for 2.5 min with 4% paraformaldehyde at 4°C. After blocking Fc receptors with CD16/CD32 Fc block (eBioscience) for 5 min, cells were permeabilized with permeabilization buffer (eBioscience) and incubated with the V5-555 antibody (1:100 in permeabilization buffer). After washing in permeabilization buffer and subsequently in FACS buffer, nuclei were counterstained with DAPI, and coverslips were mounted in fluorescent mounting medium (Dako). Images were acquired with an LSM 780 Axio Imager 2 confocal microscope using a 63× objective.

For immunohistochemistry, spleens were fixed in PBS with 4% paraformaldehyde for 1 h at 4°C and cryo-protected in PBS with 30% sucrose before being embedded in optimal cutting temperature compound (Sakura). Frozen spleens were sectioned (14-µm thickness) on a microtome and fixed in acetone. For immunostaining, all incubations were performed in a humidified chamber at room temperature. Sections were washed and blocked in FACS buffer and CD16/CD32 Fc block (eBioscience) for 15 min. The following antibodies and reagents were used for

immunostaining: anti–CD21-FITC (BD Biosciences), anti–CD23-APC (Biolegend), anti–MOMA1-biotin (Abcam), and Streptavidin-PE (Biolegend). Images were acquired with an LSM 780 Axio Imager 2 confocal microscope using a 25× objective and a 4 × 4 tile scan.

In vitro plasmablast differentiation assays

For LPS-induced plasmablast differentiation assays, splenic B220$^+$ B cells were enriched using MACS technology (Miltenyi Biotec) according to the manufacturer's instructions. Purified B cells were plated at a density of 150,000 cells/ml in IMDM (Life Technologies) supplemented with 10% fetal calf serum (Sigma), 50 µM 2-mercaptoethanol, 2 mM glutamine (Gibco), 100 U/ml penicillin (Sigma), and 100 µg/ml streptomycin sulfate (Sigma) and were subsequently treated for up to 4 d with 25 µg/ml LPS (Sigma). For the iGB cell differentiation system (Nojima et al., 2011; Wöhner et al., 2016), 40LB stromal cells (cultured in DMEM supplemented with 10% fetal calf serum) were inactivated by irradiation. 100,000 splenic B cells, which were enriched using CD43 MACS beads (Miltenyi Biotec), were plated onto the 40LB cells in 6-well plates in RPMI medium (supplemented with 10% fetal calf serum [ThermoFisher Scientific; lot42A0368K], 1 mM glutamine, 50 µM 2-mercaptoethanol, 10 mM Hepes, and 1 mM sodium pyruvate) and stimulated with recombinant IL-4 (20 ng/ml) for 4 d. At day 4, 100,000 stimulated B cells were transferred onto fresh 40LB cells in a 6-well plate and stimulated with recombinant IL-21 (10 ng/ml) for another 4 d until cells were analyzed by flow cytometry.

Quantitative RT-PCR (qRT-PCR) and RT-PCR analysis

Tissues and cells were isolated and homogenized in TRIzol reagent (Invitrogen). Total RNA was isolated according to the manufacturer's instructions. RNA was reverse transcribed with the iScript cDNA synthesis kit (Bio-Rad). Real-time PCR analysis was performed with GoTaq qPCR master mix (Promega) on a CFX384 system (Bio-Rad). Data were normalized to values for the housekeeping gene *Gapdh* for mouse samples and *ACTB* for human samples. All primers used in this study are listed in Table S1. Mouse *Xbp1s* and *Xbp1u* mRNA levels were monitored by semiquantitative RT-PCR using cDNA synthesized from RNA as described above with OneTaq Hot Start PCR Reaction Mix (New England Biolabs) for 26 cycles (see Table S1 for RT-PCR primer sequences). PCR products were resolved by 3% agarose gel electrophoresis.

QuantSeq 3′ mRNA sequencing and data analysis

cDNA libraries for each of the samples were generated from 500 ng of total RNA using the QuantSeq 3′ mRNA-Seq Library Prep Kit (FWD) for Illumina (Lexogen) following the manufacturer's instructions. QuantSeq generates highly strand-specific next-generation sequencing libraries close to the 3′ end of polyadenylated RNA. Briefly, the first cDNA strand was generated through reverse transcription initiated by oligo(dT) priming. Synthesis of the second cDNA strand was performed by random priming in a manner that DNA polymerase was efficiently stopped when reaching the next hybridized random primer, so only the fragment closest to the 3′ end got extended until the end and got both the adapter sequences necessary for PCR amplification. SR100 sequencing was performed on HiSeq 2500 at the Vienna BioCenter Core Facilities (VBCF) Next-Generation Sequencing Facility using v4 SBS reagents. Trimming was performed using BBDuk v36.92 (ref = poly-A.fa.gz,truseq.fa.gz k = 13 ktrim = r forcetrimleft = 11 use-shortkmers = t mink = 5 qtrim = t trimq = 10 minlength = 30). Reads mapping to mouse ribosomal RNA transcripts (refseq) were removed using bwa v0.7.12 alignment and samtools v1.3.1. Remaining reads were aligned to the mouse genome mm10 using TopHat v2.1.1 (parameter: –library-type fr-secondstrand), and reads in genes were counted with htseq-count v0.6.1 (parameter: -s yes; reference data: illumina iGenomes, UCSC; mm10). DESeq2 v1.18.1 in R v3.4.0 was used to perform differential expression analysis using recommended minimal gene prefiltering (keeping genes with at least 10 reads total). Counts per million were computed using edgeR v3.20.1; counts per million gene expression values were transformed into log space and scaled (by gene) to mean 0 and unit standard deviation before heatmap visualization. Enriched GO terms were determined using DAVID v6.7 (https://david.ncifcrf.gov). The data discussed in this publication have been deposited in NCBI's Gene Expression Omnibus (Edgar et al., 2002) and are accessible through GEO Series accession no. GSE141629.

Protein isolation and immunoblotting

For protein extraction, cells or tissues were manually homogenized in Hunt buffer (20 mM Tris-HCl, pH 8.0, 100 mM sodium chloride, 1 mM EDTA, and 0.5% NP-40) supplemented with Halt protease/phosphatase inhibitor cocktail (ThermoFisher Scientific). After full-speed centrifugation, the supernatant containing the soluble protein fraction was further used. Equal amounts of 20–30 µg of proteins were separated by SDS-PAGE and transferred onto polyvinylidene fluoride membranes (Immobilion-P, Merck Millipore) according to standard protocols. Blots were blocked for 1 h with 5% milk in TBST (1× Tris-buffered saline and 0.1% Tween-20) and were then incubated overnight at 4°C with primary antibodies diluted in 5% milk in TBST. Blots were washed three times in TBST for 5 min and were then incubated with HRP-conjugated secondary anti-mouse-IgG-H&L chain (Promega) or anti-rabbit-IgG-F(ab′)2 (GE Healthcare) antibody for 1 h at room temperature, washed three times in TBST for 5 min, and visualized using enhanced chemiluminescence (GE Healthcare). See Table S2 for a list of antibodies used in this study. β-Actin was used to control for protein loading. IgM was detected by incubating blots for 1 h with HRP-conjugated secondary anti-mouse-IgG-H&L chain (GE Healthcare).

Electron microscopy

Electron microscopy was performed by the EM Facility of the VBCF, a member of the Vienna BioCenter, Austria. B220$^+$ B cells were stimulated for 4 d with LPS and then pelleted for 3 min at 500 *g*, washed in prewarmed PBS, and then fixed using prewarmed 2.5% glutaraldehyde in in 0.1 mol/liter sodium phosphate buffer, pH 7.4, for 1 h. Samples were then rinsed with the same buffer, post-fixed in 1% osmium tetroxide in 0.1 mol/liter

sodium phosphate buffer, pH 7.4, on ice, dehydrated in a graded series of acetone on ice, and embedded in Agar 100 resin. 70-nm sections were cut parallel to the substrate and post-stained with 2% uranyl acetate and Reynolds lead citrate. Sections were examined with a FEI Morgagni 268D operated at 80 kV. Images were acquired using an 11-megapixel Morada CCD camera (Olympus-SIS).

Neutrophil antibody-binding assays

For serum antibody-binding assays, BM from femurs and tibias of *Rag2*-deficient mice was isolated. After red blood cell lysis (ammonium-chloride-potassium buffer incubation), two million cells were incubated with the indicated dilutions from control or *Jagn1*$^{\Delta B}$ sera for 10 min on ice with and without previously blocking Fc receptors with Fc-blocking antibodies (eBioscience). After two washing steps in PBS, cells were stained with anti-mouse IgG F(ab)$_2$-PE (eBioscience; 1:1,000 in PBS) for 15 min and then washed again in PBS. After blocking Fc receptors with CD16/CD32 Fc block (eBioscience) in all samples, cells were stained with Ly6G-FITC or Ly6G-PE-Cy7 and CD11b-BV510 (all Biolegend; 1:500), washed in FACS buffer, filtered, and analyzed for IgG binding to Fc receptors on CD11b$^+$Ly6G$^+$ neutrophils and CD11b$^+$Ly6G$^-$ myeloid cells, including monocytes.

E0771 cancer cell–killing experiments

E0771 breast cancer cells were orthotopically injected in control and *Jagn1*$^{\Delta B}$ mice as previously described (Ewens et al., 2005). In brief, cells were harvested for injection into mice by trypsin digestion for 5 min, washed in HBSS, counted, diluted in this salt solution, and orthotopically injected into the fat pad of the mammary gland (250,000 cells/100 µl 1:1 diluted in Matrigel [Corning]). Sera of tumor-bearing mice were harvested before they were sacrificed following the ethical guidelines. For the ADCC experiments, 10,000 E0771 cells were plated in a total of 50 µl RPMI-based medium (supplemented with 10% fetal calf serum, 1 mM glutamine, 50 µM 2-mercaptoethanol, 10 mM Hepes, 1 mM sodium pyruvate, 100 U/ml penicillin, and 100 µg/ml streptomycin sulfate) per well in 96-well plates containing either 20 µl serum or 1 µg purified IgG from control and *Jagn1*$^{\Delta B}$ E0771 tumor–bearing mice. After 2-h opsonization, either *Rag2*-deficient BM cells (containing 50% neutrophils) or freshly isolated Ly6G-enriched BM neutrophils using MACS (Miltenyi Biotec) were added at increasing E/T ratios for 4 h. Cell viability of Ly6G$^-$ FSC^{high} tumor cells was assessed with the Fixable Viability Dye eFluor780 (eBioscience), and IgG binding to tumor cells was confirmed by staining with anti-mouse IgG F(ab)$_2$-PE (eBioscience).

Epstein-Barr virus–transformed lymphoblastoid cell lines

To generate Epstein-Barr virus–transformed lymphoblastoid cell lines, B cells from healthy individuals and *JAGN1* mutant patients were isolated and infected with Epstein-Barr virus as described previously (Boztug et al., 2014). Experiments with human biological samples were done upon informed consent and approval by the Ludwig Maximilians University ethics board, respecting current regulatory frameworks.

Assessment of genetic contributions in mixed backgrounds

The genomic proportion of C57BL/6J, 129/Sv, and BALB/c was determined by simple sequence length polymorphisms (also called microsatellites)–based screening of the mouse genetic background. The PCR screening was achieved by using sets of ∼92 markers evenly dispersed at a distance of 20 cM (∼20–40 Mbases) over the 19 autosomal chromosomes. To analyze PCR products, capillary-based electrophoresis runs on a fragment analyzer were used.

Statistics

All values are given as means ± SD. Comparisons between two groups were analyzed using unpaired Student's *t* tests and corrected for multiple comparisons using the Holm-Sidak method. Comparisons between groups over different time points (Fig. 1 D and Fig. S5 A) or dilutions (Fig. 1 B) were analyzed by two-way ANOVA with Bonferroni correction. Comparisons between four groups (Fig. 4 G) were analyzed by one-way ANOVA followed by Bonferroni correction. P values were calculated with GraphPad Prism software: *, $P < 0.05$; **, $P < 0.01$; ***, $P < 0.001$.

Online supplemental material

Fig. S1 excludes *Mb1*-Cre effects and confirms the *Jagn1* KO phenotype using *Cd23*-Cre–mediated deletion of *Jagn1*. Fig. S2 shows assessment of *Jagn1* deletion, JAGN1 subcellular localization, and characterization of *Jagn1*$^{\Delta B}$ plasma cells. Fig. S3 illustrates phenotypic effects of *Jagn1* deletion on B cell homeostasis and plasma cell levels in mixed genetic backgrounds. Fig. S4 reports differentially expressed genes, affected organelles, and IgM levels in in vitro–generated *Jagn1*-deficient plasmablasts. Fig. S5 shows in vivo stability, target cell binding, and complement C3 binding of control versus *Jagn1*$^{\Delta B}$ antibodies. Table S1 lists primers used for genotyping and gene expression analysis in this study. Table S2 provides details of the antibodies used in this study.

Acknowledgments

We thank all members of the Penninger laboratory for helpful discussions and technical support. Moreover, we thank all members of the Research Institute of Molecular Pathology–Institute of Molecular Biotechnology of the Austrian Academy of Sciences (IMBA) bio-optics service facility for assistance in cell sorting as well as the Molecular Biology Service, VBCF Electron Microscopy Facility, the VBCF Next-Generation Sequencing Facility, and the VBCF Histopathology Facility. We also thank Laurie Glimcher (Dana-Farber Cancer Institute, Harvard Medical School, Boston, MA) and her laboratory for kindly providing the *Ire1*$^{\Delta hem}$ mouse sera. Moreover, we would like to thank Sabine Jurado, Rene Rauschmeier, and other members of the Busslinger laboratory for their assistance and advice. Furthermore, we thank Christian Theussl for cryopreservation of mouse lines, in vitro fertilization, and rederivation of mice from frozen sperm.

J.M. Penninger is supported by grants from IMBA, the Austrian Ministry of Sciences, the Austrian Academy of Sciences, the T. von Zastrow Foundation, the FWF Wittgenstein award (Z 271-B19), and a Canada 150 Chair.

Author contributions: Immune phenotyping, generation of BM chimeras, and flow cytometry experiments were performed and analyzed by A. Hagelkruys and G. Wirnsberger. The OVA immunization was carried out and analyzed by L. Tortola and G. Wirnsberger, the NP-KLH immunization by M. Wöhner and A. Hagelkruys, and the VSV infections by B. Vilagos and A. Bergthaler. J. Stadlmann performed all the MS analyses. Ig isotyping, immunofluorescence, immunohistochemistry, quantitative PCR analysis, immunoblots, and in vitro LPS-stimulated plasmablast differentiations were performed by A. Hagelkruys. M. Wöhner and A. Hagelkruys carried out the iGB experiments, and M. Wöhner performed the ELISPOT assays and IgG1 ELISAs. M. Horrer, G. Jonsson, and M. Kogler helped with immunophenotyping and flow cytometry. R. Koglgruber assisted with mouse genotyping. D. Hoffmann prepared the libraries for the QuantSeq experiment; M. Novatchkova analyzed the sequencing data. P. Bönelt and M. Busslinger generated the *Rosa26*-EGFP mice used in this study. U. Steffen and G. Schett performed experiments with human macrophages. C. Klein designed the experiments with human patients and provided samples. A. Hagelkruys, G. Wirnsberger, and J.M. Penninger conceptualized and designed the experiments and wrote the manuscript with input from the co-authors.

Disclosures: The authors declare no competing interests exist.

Submitted: 25 March 2020
Revised: 17 July 2020
Accepted: 18 August 2020

References

Ackerman, M.E., M. Crispin, X. Yu, K. Baruah, A.W. Boesch, D.J. Harvey, A.-S. Dugast, E.L. Heizen, A. Ercan, I. Choi, et al. 2013. Natural variation in Fc glycosylation of HIV-specific antibodies impacts antiviral activity. *J. Clin. Invest.* 123:2183–2192. https://doi.org/10.1172/JCI65708

Arnold, J.N., M.R. Wormald, R.B. Sim, P.M. Rudd, and R.A. Dwek. 2007. The impact of glycosylation on the biological function and structure of human immunoglobulins. *Annu. Rev. Immunol.* 25:21–50. https://doi.org/10.1146/annurev.immunol.25.022106.141702

Baris, S., E. Karakoc-Aydiner, A. Ozen, K. Delil, A. Kiykim, I. Ogulur, I. Baris, and I.B. Barlan. 2015. JAGN1 Deficient Severe Congenital Neutropenia: Two Cases from the Same Family. *J. Clin. Immunol.* 35:339–343. https://doi.org/10.1007/s10875-015-0156-2

Benner, R., W. Hijmans, and J.J. Haaijman. 1981. The bone marrow: the major source of serum immunoglobulins, but still a neglected site of antibody formation. *Clin. Exp. Immunol.* 46:1–8.

Bettigole, S.E., R. Lis, S. Adoro, A.-H. Lee, L.A. Spencer, P.F. Weller, and L.H. Glimcher. 2015. The transcription factor XBP1 is selectively required for eosinophil differentiation. *Nat. Immunol.* 16:829–837. https://doi.org/10.1038/ni.3225

Bondt, A., M.H.J. Selman, A.M. Deelder, J.M.W. Hazes, S.P. Willemsen, M. Wuhrer, and R.J.E.M. Dolhain. 2013. Association between galactosylation of immunoglobulin G and improvement of rheumatoid arthritis during pregnancy is independent of sialylation. *J. Proteome Res.* 12:4522–4531. https://doi.org/10.1021/pr400589m

Boztug, K., P.M. Järvinen, E. Salzer, T. Racek, S. Mönch, W. Garncarz, E.M. Gertz, A.A. Schäffer, A. Antonopoulos, S.M. Haslam, et al. 2014. JAGN1 deficiency causes aberrant myeloid cell homeostasis and congenital neutropenia. *Nat. Genet.* 46:1021–1027. https://doi.org/10.1038/ng.3069

Brewer, J.W., L.M. Hendershot, C.J. Sherr, and J.A. Diehl. 1999. Mammalian unfolded protein response inhibits cyclin D1 translation and cell-cycle progression. *Proc. Natl. Acad. Sci. USA.* 96:8505–8510. https://doi.org/10.1073/pnas.96.15.8505

Caspersen, C., P.S. Pedersen, and M. Treiman. 2000. The sarco/endoplasmic reticulum calcium-ATPase 2b is an endoplasmic reticulum stress-inducible protein. *J. Biol. Chem.* 275:22363–22372. https://doi.org/10.1074/jbc.M001569200

Chen, R., L. Shi, J. Hakenberg, B. Naughton, P. Sklar, J. Zhang, H. Zhou, L. Tian, O. Prakash, M. Lemire, et al. 2016. Analysis of 589,306 genomes identifies individuals resilient to severe Mendelian childhood diseases. *Nat. Biotechnol.* 34:531–538. https://doi.org/10.1038/nbt.3514

de Haan, N., K.R. Reiding, G. Driessen, M. van der Burg, and M. Wuhrer. 2016. Changes in Healthy Human IgG Fc-Glycosylation after Birth and during Early Childhood. *J. Proteome Res.* 15:1853–1861. https://doi.org/10.1021/acs.jproteome.6b00038

Edgar, R., M. Domrachev, and A.E. Lash. 2002. Gene Expression Omnibus: NCBI gene expression and hybridization array data repository. *Nucleic Acids Res.* 30:207–210. https://doi.org/10.1093/nar/30.1.207

Ewens, A., E. Mihich, and M.J. Ehrke. 2005. Distant metastasis from subcutaneously grown E0771 medullary breast adenocarcinoma. *Anticancer Res.* 25(6B):3905–3915.

Ferrara, C., S. Grau, C. Jäger, P. Sondermann, P. Brünker, I. Waldhauer, M. Hennig, A. Ruf, A.C. Rufer, M. Stihle, et al. 2011. Unique carbohydrate-carbohydrate interactions are required for high affinity binding between FcgammaRIII and antibodies lacking core fucose. *Proc. Natl. Acad. Sci. USA.* 108:12669–12674. https://doi.org/10.1073/pnas.1108455108

Hetz, C., and F.R. Papa. 2018. The Unfolded Protein Response and Cell Fate Control. *Mol. Cell.* 69:169–181. https://doi.org/10.1016/j.molcel.2017.06.017

Hibi, T., and H.M. Dosch. 1986. Limiting dilution analysis of the B cell compartment in human bone marrow. *Eur. J. Immunol.* 16:139–145. https://doi.org/10.1002/eji.1830160206

Hobeika, E., S. Thiemann, B. Storch, H. Jumaa, P.J. Nielsen, R. Pelanda, and M. Reth. 2006. Testing gene function early in the B cell lineage in mb1-cre mice. *Proc. Natl. Acad. Sci. USA.* 103:13789–13794. https://doi.org/10.1073/pnas.0605944103

Huber, R., J. Deisenhofer, P.M. Colman, M. Matsushima, and W. Palm. 1976. Crystallographic structure studies of an IgG molecule and an Fc fragment. *Nature.* 264:415–420. https://doi.org/10.1038/264415a0

Jefferis, R. 2009. Glycosylation as a strategy to improve antibody-based therapeutics. *Nat. Rev. Drug Discov.* 8:226–234. https://doi.org/10.1038/nrd2804

Jennewein, M.F., and G. Alter. 2017. The Immunoregulatory Roles of Antibody Glycosylation. *Trends Immunol.* 38:358–372. https://doi.org/10.1016/j.it.2017.02.004

Kallies, A., J. Hasbold, D.M. Tarlinton, W. Dietrich, L.M. Corcoran, P.D. Hodgkin, and S.L. Nutt. 2004. Plasma cell ontogeny defined by quantitative changes in blimp-1 expression. *J. Exp. Med.* 200:967–977. https://doi.org/10.1084/jem.20040973

Kellner, C., A. Otte, E. Cappuzzello, K. Klausz, and M. Peipp. 2017. Modulating Cytotoxic Effector Functions by Fc Engineering to Improve Cancer Therapy. *Transfus. Med. Hemother.* 44:327–336. https://doi.org/10.1159/000479980

Koizumi, N., T. Ujino, H. Sano, and M.J. Chrispeels. 1999. Overexpression of a gene that encodes the first enzyme in the biosynthesis of asparagine-linked glycans makes plants resistant to tunicamycin and obviates the tunicamycin-induced unfolded protein response. *Plant Physiol.* 121:353–361. https://doi.org/10.1104/pp.121.2.353

Kornfeld, R., and S. Kornfeld. 1985. Assembly of asparagine-linked oligosaccharides. *Annu. Rev. Biochem.* 54:631–664. https://doi.org/10.1146/annurev.bi.54.070185.003215

Kwon, K., C. Hutter, Q. Sun, I. Bilic, C. Cobaleda, S. Malin, and M. Busslinger. 2008. Instructive role of the transcription factor E2A in early B lymphopoiesis and germinal center B cell development. *Immunity.* 28:751–762. https://doi.org/10.1016/j.immuni.2008.04.014

Lee, S., and L. Cooley. 2007. Jagunal is required for reorganizing the endoplasmic reticulum during Drosophila oogenesis. *J. Cell Biol.* 176:941–952. https://doi.org/10.1083/jcb.200701048

Lee, A.-H., N.N. Iwakoshi, and L.H. Glimcher. 2003. XBP-1 regulates a subset of endoplasmic reticulum resident chaperone genes in the unfolded protein response. *Mol. Cell. Biol.* 23:7448–7459. https://doi.org/10.1128/MCB.23.21.7448-7459.2003

Lei, K., and R.J. Davis. 2003. JNK phosphorylation of Bim-related members of the Bcl2 family induces Bax-dependent apoptosis. *Proc. Natl. Acad. Sci. USA.* 100:2432–2437. https://doi.org/10.1073/pnas.0438011100

Lin, C.-W., M.-H. Tsai, S.-T. Li, T.-I. Tsai, K.-C. Chu, Y.-C. Liu, M.-Y. Lai, C.-Y. Wu, Y.-C. Tseng, S.S. Shivatare, et al. 2015. A common glycan structure on immunoglobulin G for enhancement of effector functions. *Proc. Natl. Acad. Sci. USA.* 112:10611–10616. https://doi.org/10.1073/pnas.1513456112

Manz, R.A., A. Thiel, and A. Radbruch. 1997. Lifetime of plasma cells in the bone marrow. *Nature.* 388:133–134. https://doi.org/10.1038/40540

Maresch, D., and F. Altmann. 2016. Isotype-specific glycosylation analysis of mouse IgG by LC-MS. *Proteomics*. 16:1321–1330. https://doi.org/10.1002/pmic.201500367

McGehee, A.M., S.K. Dougan, E.J. Klemm, G. Shui, B. Park, Y.-M. Kim, N. Watson, M.R. Wenk, H.L. Ploegh, and C.-C.A. Hu. 2009. XBP-1-deficient plasmablasts show normal protein folding but altered glycosylation and lipid synthesis. *J. Immunol.* 183:3690–3699. https://doi.org/10.4049/jimmunol.0900953

Miletic, V.D., and M.M. Frank. 1995. Complement-immunoglobulin interactions. *Curr. Opin. Immunol.* 7:41–47. https://doi.org/10.1016/0952-7915(95)80027-1

Minnich, M., H. Tagoh, P. Bönelt, E. Axelsson, M. Fischer, B. Cebolla, A. Tarakhovsky, S.L. Nutt, M. Jaritz, and M. Busslinger. 2016. Multifunctional role of the transcription factor Blimp-1 in coordinating plasma cell differentiation. *Nat. Immunol.* 17:331–343. https://doi.org/10.1038/ni.3349

Nimmerjahn, F., and J.V. Ravetch. 2008. Fcgamma receptors as regulators of immune responses. *Nat. Rev. Immunol.* 8:34–47. https://doi.org/10.1038/nri2206

Nojima, T., K. Haniuda, T. Moutai, M. Matsudaira, S. Mizokawa, I. Shiratori, T. Azuma, and D. Kitamura. 2011. In-vitro derived germinal centre B cells differentially generate memory B or plasma cells in vivo. *Nat. Commun.* 2:465. https://doi.org/10.1038/ncomms1475

Ogilvy, S., D. Metcalf, C.G. Print, M.L. Bath, A.W. Harris, and J.M. Adams. 1999. Constitutive Bcl-2 expression throughout the hematopoietic compartment affects multiple lineages and enhances progenitor cell survival. *Proc. Natl. Acad. Sci. USA*. 96:14943–14948. https://doi.org/10.1073/pnas.96.26.14943

Okazaki, A., E. Shoji-Hosaka, K. Nakamura, M. Wakitani, K. Uchida, S. Kakita, K. Tsumoto, I. Kumagai, and K. Shitara. 2004. Fucose depletion from human IgG1 oligosaccharide enhances binding enthalpy and association rate between IgG1 and FcgammaRIIIa. *J. Mol. Biol.* 336:1239–1249. https://doi.org/10.1016/j.jmb.2004.01.007

Pučić, M., A. Knezević, J. Vidic, B. Adamczyk, M. Novokmet, O. Polasek, O. Gornik, S. Supraha-Goreta, M.R. Wormald, I. Redzić, et al. 2011. High throughput isolation and glycosylation analysis of IgG-variability and heritability of the IgG glycome in three isolated human populations. *Mol. Cell Proteomics*. 10:M111.010090. . https://doi.org/10.1074/mcp.M111.010090

Raju, T.S., J.B. Briggs, S.M. Borge, and A.J. Jones. 2000. Species-specific variation in glycosylation of IgG: evidence for the species-specific sialylation and branch-specific galactosylation and importance for engineering recombinant glycoprotein therapeutics. *Glycobiology*. 10:477–486. https://doi.org/10.1093/glycob/10.5.477

Seeling, M., C. Brückner, and F. Nimmerjahn. 2017. Differential antibody glycosylation in autoimmunity: sweet biomarker or modulator of disease activity? *Nat. Rev. Rheumatol.* 13:621–630. https://doi.org/10.1038/nrrheum.2017.146

Serebrenik, Y.V., D. Hellerschmied, M. Toure, F. López-Giráldez, D. Brookner, and C.M. Crews. 2018. Targeted protein unfolding uncovers a Golgi-specific transcriptional stress response. *Mol. Biol. Cell*. 29:1284–1298. https://doi.org/10.1091/mbc.E17-11-0693

Shields, R.L., J. Lai, R. Keck, L.Y. O'Connell, K. Hong, Y.G. Meng, S.H.A. Weikert, and L.G. Presta. 2002. Lack of fucose on human IgG1 N-linked oligosaccharide improves binding to human Fcgamma RIII and antibody-dependent cellular toxicity. *J. Biol. Chem.* 277:26733–26740. https://doi.org/10.1074/jbc.M202069200

Shinkawa, T., K. Nakamura, N. Yamane, E. Shoji-Hosaka, Y. Kanda, M. Sakurada, K. Uchida, H. Anazawa, M. Satoh, M. Yamasaki, et al. 2003. The absence of fucose but not the presence of galactose or bisecting N-acetylglucosamine of human IgG1 complex-type oligosaccharides shows the critical role of enhancing antibody-dependent cellular cytotoxicity. *J. Biol. Chem.* 278:3466–3473. https://doi.org/10.1074/jbc.M210665200

Slifka, M.K., M. Matloubian, and R. Ahmed. 1995. Bone marrow is a major site of long-term antibody production after acute viral infection. *J. Virol.* 69:1895–1902. https://doi.org/10.1128/JVI.69.3.1895-1902.1995

Slifka, M.K., R. Antia, J.K. Whitmire, and R. Ahmed. 1998. Humoral immunity due to long-lived plasma cells. *Immunity*. 8:363–372. https://doi.org/10.1016/S1074-7613(00)80541-5

Smith, K.G., A. Light, G.J. Nossal, and D.M. Tarlinton. 1997. The extent of affinity maturation differs between the memory and antibody-forming cell compartments in the primary immune response. *EMBO J.* 16:2996–3006. https://doi.org/10.1093/emboj/16.11.2996

Sriburi, R., S. Jackowski, K. Mori, and J.W. Brewer. 2004. XBP1: a link between the unfolded protein response, lipid biosynthesis, and biogenesis of the endoplasmic reticulum. *J. Cell Biol.* 167:35–41. https://doi.org/10.1083/jcb.200406136

Stadlmann, J., M. Pabst, D. Kolarich, R. Kunert, and F. Altmann. 2008. Analysis of immunoglobulin glycosylation by LC-ESI-MS of glycopeptides and oligosaccharides. *Proteomics*. 8:2858–2871. https://doi.org/10.1002/pmic.200700968

Stadlmann, J., A. Weber, M. Pabst, H. Anderle, R. Kunert, H.J. Ehrlich, H. P., Schwarz, and F. Altmann. 2009. A close look at human IgG sialylation and subclass distribution after lectin fractionation. *Proteomics*. 9:4143–4153. https://doi.org/10.1002/pmic.200800931

Stavnezer, J., J.E.J. Guikema, and C.E. Schrader. 2008. Mechanism and regulation of class switch recombination. *Annu. Rev. Immunol.* 26:261–292. https://doi.org/10.1146/annurev.immunol.26.021607.090248

Takahashi, N., I. Ishii, H. Ishihara, M. Mori, S. Tejima, R. Jefferis, S. Endo, and Y. Arata. 1987. Comparative structural study of the N-linked oligosaccharides of human normal and pathological immunoglobulin G. *Biochemistry*. 26:1137–1144. https://doi.org/10.1021/bi00378a023

Tao, M.H., and S.L. Morrison. 1989. Studies of aglycosylated chimeric mouse-human IgG. Role of carbohydrate in the structure and effector functions mediated by the human IgG constant region. *J. Immunol.* 143:2595–2601.

Taubenheim, N., D.M. Tarlinton, S. Crawford, L.M. Corcoran, P.D. Hodgkin, and S.L. Nutt. 2012. High rate of antibody secretion is not integral to plasma cell differentiation as revealed by XBP-1 deficiency. *J. Immunol.* 189:3328–3338. https://doi.org/10.4049/jimmunol.1201042

Tellier, J., W. Shi, M. Minnich, Y. Liao, S. Crawford, G.K. Smyth, A. Kallies, M. Busslinger, and S.L. Nutt. 2016. Blimp-1 controls plasma cell function through the regulation of immunoglobulin secretion and the unfolded protein response. *Nat. Immunol.* 17:323–330. https://doi.org/10.1038/ni.3348

Tournier, C., P. Hess, D.D. Yang, J. Xu, T.K. Turner, A. Nimnual, D. Bar-Sagi, S.N. Jones, R.A. Flavell, and R.J. Davis. 2000. Requirement of JNK for stress-induced activation of the cytochrome c-mediated death pathway. *Science*. 288:870–874. https://doi.org/10.1126/science.288.5467.870

Tsiantoulas, D., M. Kiss, B. Bartolini-Gritti, A. Bergthaler, Z. Mallat, H. Jumaa, and C.J. Binder. 2017. Secreted IgM deficiency leads to increased BCR signaling that results in abnormal splenic B cell development. *Sci. Rep.* 7:3540–3549. https://doi.org/10.1038/s41598-017-03688-8

Turner, M.J., E.R. Jellison, E.G. Lingenheld, L. Puddington, and L. Lefrançois. 2008. Avidity maturation of memory CD8 T cells is limited by self-antigen expression. *J. Exp. Med.* 205:1859–1868. https://doi.org/10.1084/jem.20072390

Urano, F., X. Wang, A. Bertolotti, Y. Zhang, P. Chung, H.P. Harding, and D. Ron. 2000. Coupling of stress in the ER to activation of JNK protein kinases by transmembrane protein kinase IRE1. *Science*. 287:664–666. https://doi.org/10.1126/science.287.5453.664

Vidarsson, G., G. Dekkers, and T. Rispens. 2014. IgG subclasses and allotypes: from structure to effector functions. *Front. Immunol.* 5:520. https://doi.org/10.3389/fimmu.2014.00520

Wiest, D.L., J.K. Burkhardt, S. Hester, M. Hortsch, D.I. Meyer, and Y. Argon. 1990. Membrane biogenesis during B cell differentiation: most endoplasmic reticulum proteins are expressed coordinately. *J. Cell Biol.* 110:1501–1511. https://doi.org/10.1083/jcb.110.5.1501

Wirnsberger, G., F. Zwolanek, J. Stadlmann, L. Tortola, S.W. Liu, T. Perlot, P. Järvinen, G. Dürnberger, I. Kozieradzki, R. Sarao, et al. 2014. Jagunal homolog 1 is a critical regulator of neutrophil function in fungal host defense. *Nat. Genet.* 46:1028–1033. https://doi.org/10.1038/ng.3070

Wöhner, M., H. Tagoh, I. Bilic, M. Jaritz, D.K. Poliakova, M. Fischer, and M. Busslinger. 2016. Molecular functions of the transcription factors E2A and E2-2 in controlling germinal center B cell and plasma cell development. *J. Exp. Med.* 213:1201–1221. https://doi.org/10.1084/jem.20152002

Woof, J.M., and D.R. Burton. 2004. Human antibody-Fc receptor interactions illuminated by crystal structures. *Nat. Rev. Immunol.* 4:89–99. https://doi.org/10.1038/nri1266

Yoshida, H., T. Matsui, A. Yamamoto, T. Okada, and K. Mori. 2001. XBP1 mRNA is induced by ATF6 and spliced by IRE1 in response to ER stress to produce a highly active transcription factor. *Cell*. 107:881–891. https://doi.org/10.1016/S0092-8674(01)00611-0

Zhang, K., H.N. Wong, B. Song, C.N. Miller, D. Scheuner, and R.J. Kaufman. 2005. The unfolded protein response sensor IRE1alpha is required at 2 distinct steps in B cell lymphopoiesis. *J. Clin. Invest.* 115:268–281. https://doi.org/10.1172/JCI200521848

Zhang, D., B. Chen, Y. Wang, P. Xia, C. He, Y. Liu, R. Zhang, M. Zhang, and Z. Li. 2016. Disease-specific IgG Fc N-glycosylation as personalized biomarkers to differentiate gastric cancer from benign gastric diseases. *Sci. Rep.* 6:25957. https://doi.org/10.1038/srep25957

Zinszner, H., M. Kuroda, X. Wang, N. Batchvarova, R.T. Lightfoot, H. Remotti, J.L. Stevens, and D. Ron. 1998. CHOP is implicated in programmed cell death in response to impaired function of the endoplasmic reticulum. *Genes Dev.* 12:982–995. https://doi.org/10.1101/gad.12.7.982

JEM

Supplemental material

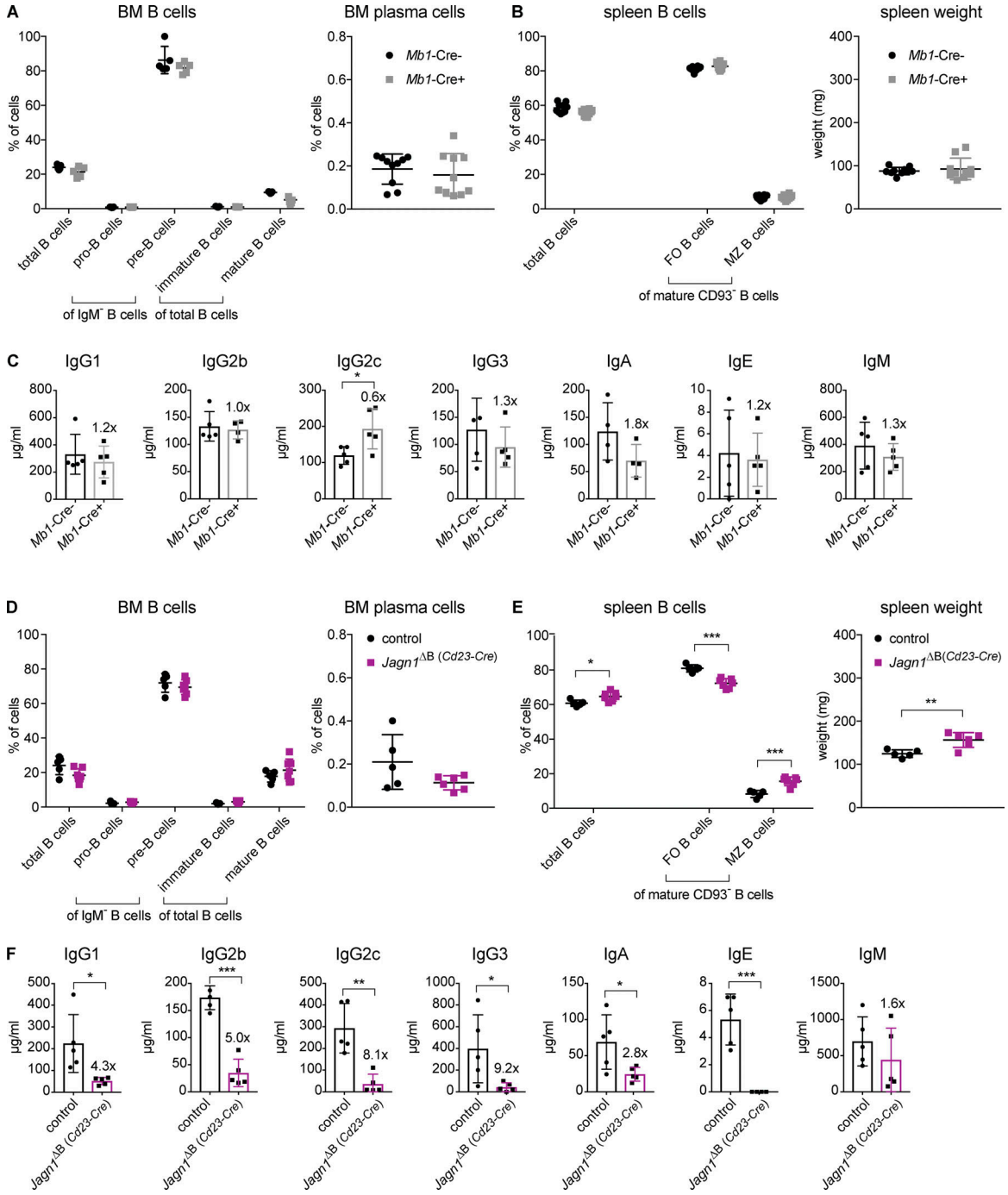

Figure S1. **Exclusion of *Mb1*-Cre effects and confirmation of the *Jagn1* KO phenotype by *Cd23*-Cre–mediated deletion of *Jagn1* regarding B cell development, B cell homeostasis, and plasma cells. (A)** B cell developmental stages among BM CD19$^+$ B cells (left panel; $n > 4$) and BM CD138$^+$CD28$^+$ plasma cells (right panel; $n > 9$) in mice of the indicated genotypes, analyzed by flow cytometry. BM B cells include total CD19$^+$ B cells, immature B cells (B220^{low}IgM$^+$), mature B cells (B220$^+$IgM$^+$), and precursor cells (IgM$^-$) divided into cKit$^+$ pro–B cells and CD2$^+$ pre–B cells. Data are shown for one of two independent experiments. **(B)** Percentages of total CD19$^+$ B cells, CD23$^+$CD21^{int} FO, and CD21$^+$CD23^{low} MZ B cells among mature CD19$^+$CD93$^-$ splenic B cells (left panel; $n > 9$). Right panel shows spleen weights from mice of the indicated genotypes ($n > 9$). Data are shown for one of two independent experiments. **(C)** Serum Ig concentrations from mice of the indicated genotypes as assessed by an isotype-multiplexing assay ($n = 5$). Fold reductions are indicated above bar diagrams. Data are shown for one of two independent experiments. **(D)** B cell developmental stages among BM CD19$^+$ B cells (left panel; $n > 4$) and BM CD138$^+$CD28$^+$ plasma cells (right panel; $n > 4$) in mice of the indicated genotypes. BM B cells include total CD19$^+$ B cells, immature B cells (B220^{low}IgM$^+$), mature B cells (B220$^+$IgM$^+$), and precursor cells (IgM$^-$), divided into cKit$^+$ pro–B cells and CD2$^+$ pre–B cells. Data are shown for one of two independent experiments. **(E)** Percentages of total splenic CD19$^+$ B cells, CD23$^+$CD21^{int} FO, and CD21$^+$CD23^{low} MZ B cells among total mature CD19$^+$CD93$^-$ B cells (left panel; $n > 4$). Right panel indicates spleen weights of mice of the indicated genotypes ($n > 4$). Data are shown for one of two independent experiments. **(F)** Ig concentrations in sera from mice of the indicated genotypes as measured by an isotype-multiplexing assay ($n = 5$). Fold reductions are indicated above bar diagrams. Data are shown for one of two independent experiments. For panels A–F, each data point represents an individual mouse. P values were calculated using the Student's *t* test and corrected for multiple comparisons using the Holm-Sidak method. *, $P < 0.05$; **, $P < 0.01$; ***, $P < 0.001$. Error bars represent means ± SD.

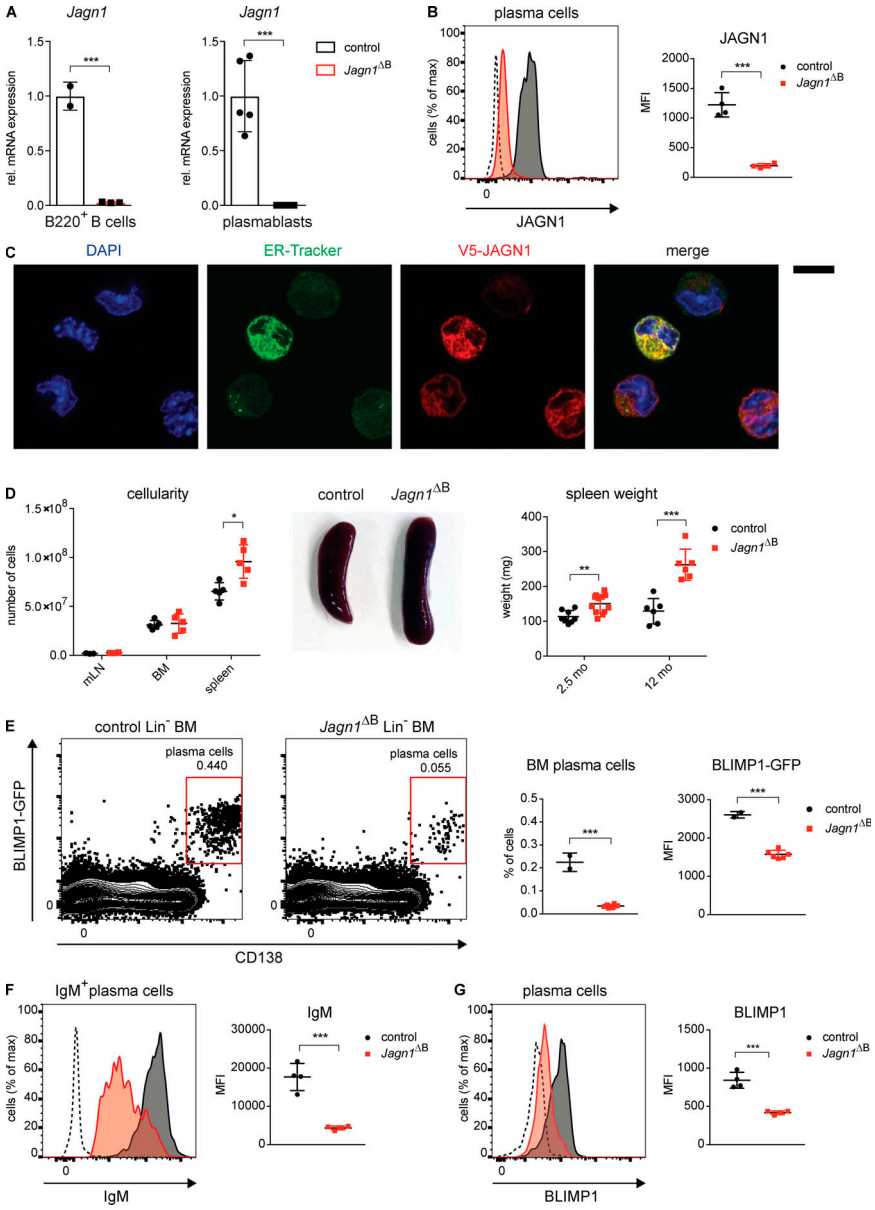

Figure S2. **Assessment of *Jagn1* deletion, JAGN1 subcellular localization, and characterization of *Jagn1*$^{\Delta B}$ plasma cells. (A)** Efficient deletion of *Jagn1* as assessed by *Jagn1* mRNA levels in splenic B220$^+$ B cells (left panel; $n = 2$) and sorted plasmablasts after 4 d of LPS stimulation (right panel; $n = 5$). mRNA levels were determined by qRT-PCR and normalized to the expression of the housekeeping gene *Gapdh*, and the average of the controls was set to 1. Data are shown for one of two independent experiments. **(B)** JAGN1 intracellular staining in splenic plasma cells. Representative histogram overlay (left panel) and mean fluorescence intensity (MFI; right panel; $n = 4$) for JAGN1 stainings of cells from mice of the indicated genotypes are shown. The dotted line in the histogram indicates adding the secondary antibody only as background control. Data are shown for one of three independent experiments. **(C)** Subcellular localization of JAGN1 (N-terminally V5 tagged) in the MPC-11 mouse plasmacytoma cell line as assessed by immunostaining for the V5 tag (red). Cells were counterstained with DAPI (blue) to image nuclei and the ER staining dye ER-Tracker (green). Magnification is indicated (scale bar = 10 µm). **(D)** Total cellularity of denoted organs (left panel; 2.5 mo of age; $n > 3$), representative pictures of spleens (middle panel; 2.5 mo of age), and spleen weights (right panel; 2.5 and 12 mo of age; $n > 5$) of mice with the indicated genotypes. mLN, mesenteric lymph node. Data are shown for one of at least two independent experiments. **(E)** Representative dot blots of CD138- and BLIMP1-GFP–positive plasma cells in lineage-negative BM cells (left panel), proportions of BM plasma cells (middle panel), and mean fluorescence intensity (MFI) of the BLIMP1-GFP reporter in these BM plasma cells (right panel) in mice of the indicated genotypes as assessed by flow cytometry (right panel; $n = 2$ and 6 mice, respectively). Lin$^-$ cells included all cells negative for the lineage markers TCRβ, CD23, CD11b, and CD49b. Data are shown for one of two independent experiments. **(F)** Intracellular levels of IgM in splenic CD28$^+$CD138$^+$IgM$^+$ plasma cells isolated from mice of the indicated genotypes. Representative histogram overlays (left panel) and mean fluorescence intensities (MFI; right panel; $n = 4$) are shown. The dotted line in the histogram indicates isotype staining as background control. Data are shown for one of two independent experiments. **(G)** Expression of BLIMP1 in splenic CD28$^+$CD138$^+$ plasma cells isolated from mice of the indicated genotypes, as assessed by intracellular staining and flow cytometry. Representative histogram overlays (left panel) and mean fluorescence intensities (MFI; right panel; $n = 4$) are shown. The dotted line in the histogram indicates the isotype background control. Data are shown for one of three independent experiments. For panels A, B, and D–G, each data point represents an individual mouse (or cells originating from an individual mouse). P values were calculated using the Student's *t* test and corrected for multiple comparisons using the Holm-Sidak method. *, $P < 0.05$; **, $P < 0.01$; ***, $P < 0.001$. Error bars represent means ± SD.

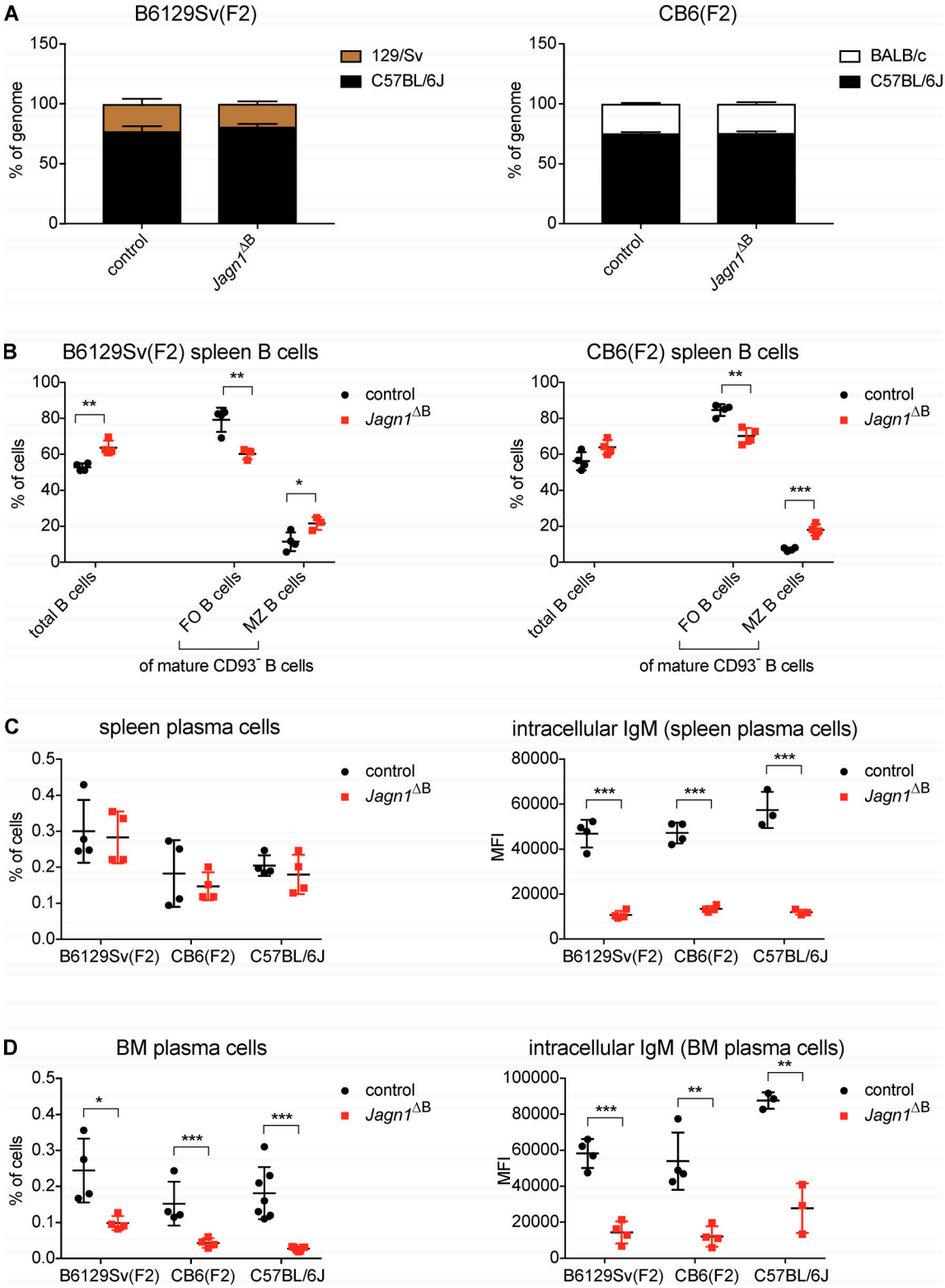

Figure S3. **Phenotypic effects of *Jagn1* deletion on B cell homeostasis and plasma cell levels in mixed genetic backgrounds. (A)** Genomic contribution of C57BL/6J (black) and 129/Sv (brown) or BALB/c (white) in F2 C57BL/6Jx129/Sv (B6129Sv; left) or F2 C57BL/6JxBALB/c (CB6; right) mice as determined by microsatellite PCR analysis ($n = 4$). **(B)** Percentages of total splenic CD19$^+$ B cells, CD23$^+$CD21^{int} FO, and CD21$^+$CD23^{low} MZ B cells among total mature splenic CD19$^+$CD93$^-$ B cells in mice of the indicated genotypes and genetic backgrounds as determined by immunostaining and flow cytometry ($n = 4$). **(C and D)** Percentages of splenic (C) and BM (D) CD138$^+$CD28$^+$ plasma cells (left panels) and mean fluorescence intensity (MFI) of intracellular IgM levels in plasma cells (right panels) in mice of the indicated genotypes and genetic backgrounds ($n > 2$). For panels B–D, each data point represents an individual mouse. Data in this figure correspond to one independent experiment. P values were calculated using the Student's *t* test and corrected for multiple comparisons using the Holm-Sidak method. *, $P < 0.05$; **, $P < 0.01$; ***, $P < 0.001$. Error bars represent means ± SD.

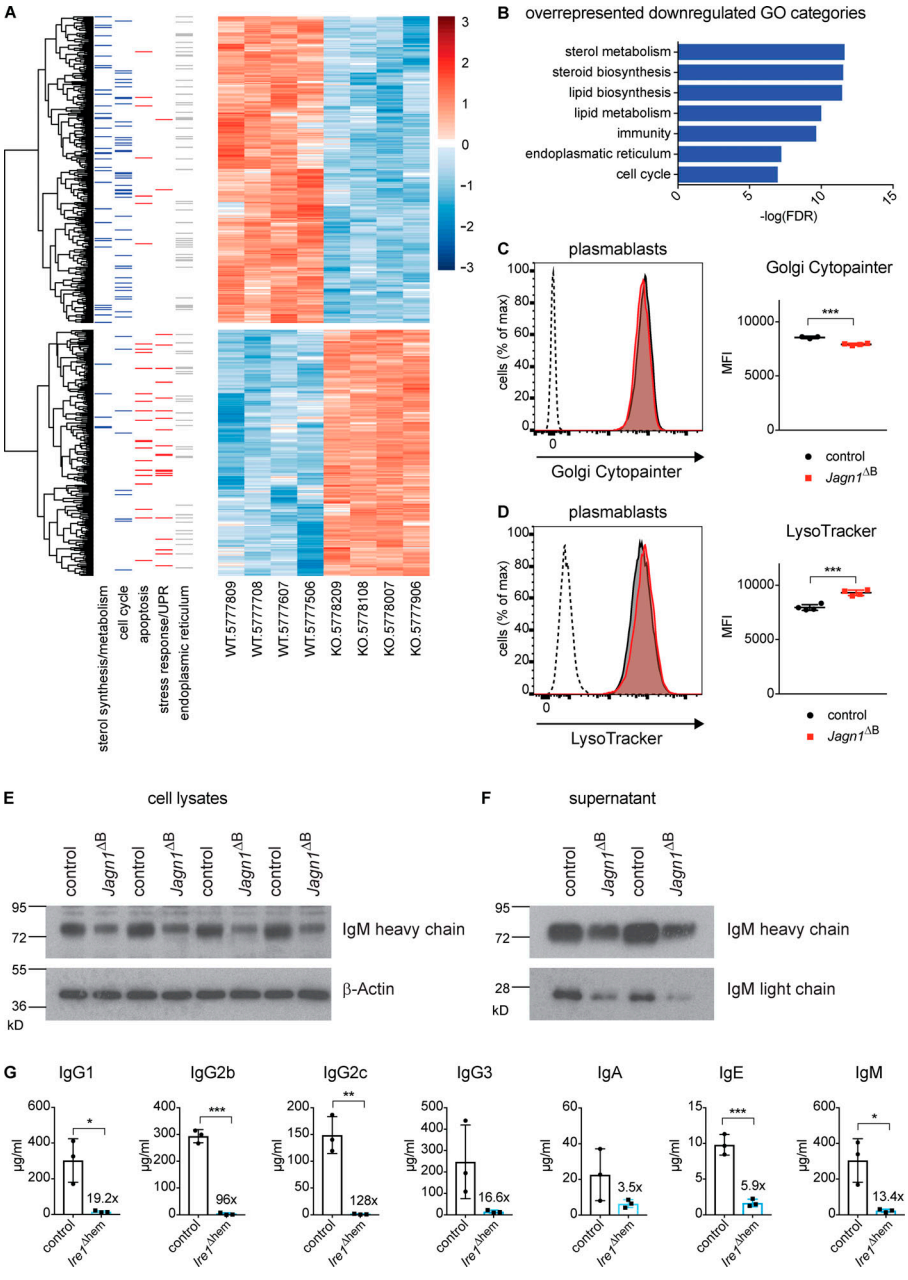

Figure S4. **Differentially expressed genes, affected organelles, and IgM levels in in vitro–generated *Jagn1*-deficient plasmablasts. (A)** Heatmap depicting relative expression levels of 521 dysregulated genes as assessed by QuantSeq 3′ mRNA sequencing of mRNA from *Jagn1*$^{\Delta B}$ (right) versus control (left) sorted plasmablasts (data from four individual mice are shown; padj < 0.01). Color gradient from blue to red indicates increased expression levels (z-score). Genes in sterol and cell cycle categories are shown by blue lines on the left and are mostly down-regulated in cells from *Jagn1*$^{\Delta B}$ mice. Genes involved in apoptosis and stress response/UPR are displayed by red lines on the left and are mostly up-regulated in cells from *Jagn1*$^{\Delta B}$ mice. Genes described with the GO keyword ER are marked by gray lines on the left. **(B)** Functional enrichment analysis of down-regulated genes determined by QuantSeq 3′ mRNA sequencing of mRNA from *Jagn1*$^{\Delta B}$ versus control plasmablasts (data from four individual mice) as assessed by DAVID GO analysis. Top GO terms enriched in *Jagn1*$^{\Delta B}$ plasmablasts ranked by the negative logarithm of the false discovery rate (FDR) are shown (padj < 0.01). **(C)** Golgi Cytopainter staining in plasmablasts ($CD22^{-}CD138^{+}$) isolated from mice of the indicated genotypes after 4 d of LPS stimulation. Representative histogram overlays (left panel) and mean fluorescence intensities (MFI; right panel; $n > 2$) are shown. The dotted line in the histogram indicates the background control. Data are shown for one of two independent experiments. **(D)** LysoTracker staining in plasmablasts ($CD22^{-}CD138^{+}$) from mice of the indicated genotypes after 4 d of LPS stimulation. Representative histogram overlays (left panel) and mean fluorescence intensities (MFI; right panel; $n = 4$) are shown. The dotted line in the histogram indicates the background control. Data are shown for one of two independent experiments. **(E)** Immunoblot analysis for IgM heavy chains on lysates prepared from sorted plasmablasts from mice of the indicated genotypes, analyzed after 4 d of LPS stimulation. β-Actin protein levels are shown as loading controls. Data are shown for one of two independent experiments. **(F)** Immunoblot analyses to test for secreted IgM heavy and light chains from supernatants of cell cultures as in C. Data are shown for one of two independent experiments. **(G)** Ig concentrations in sera from mice of the indicated genotypes ($n = 3$) assessed with an isotype-multiplexing assay. Fold reductions are indicated above bar diagrams. Data are shown for one of two independent experiments. For panels C, D, and G, each data point represents an individual mouse. P values were calculated using the Student's *t* test. *, P < 0.05; **, P < 0.01; ***, P < 0.001. Error bars represent means ± SD.

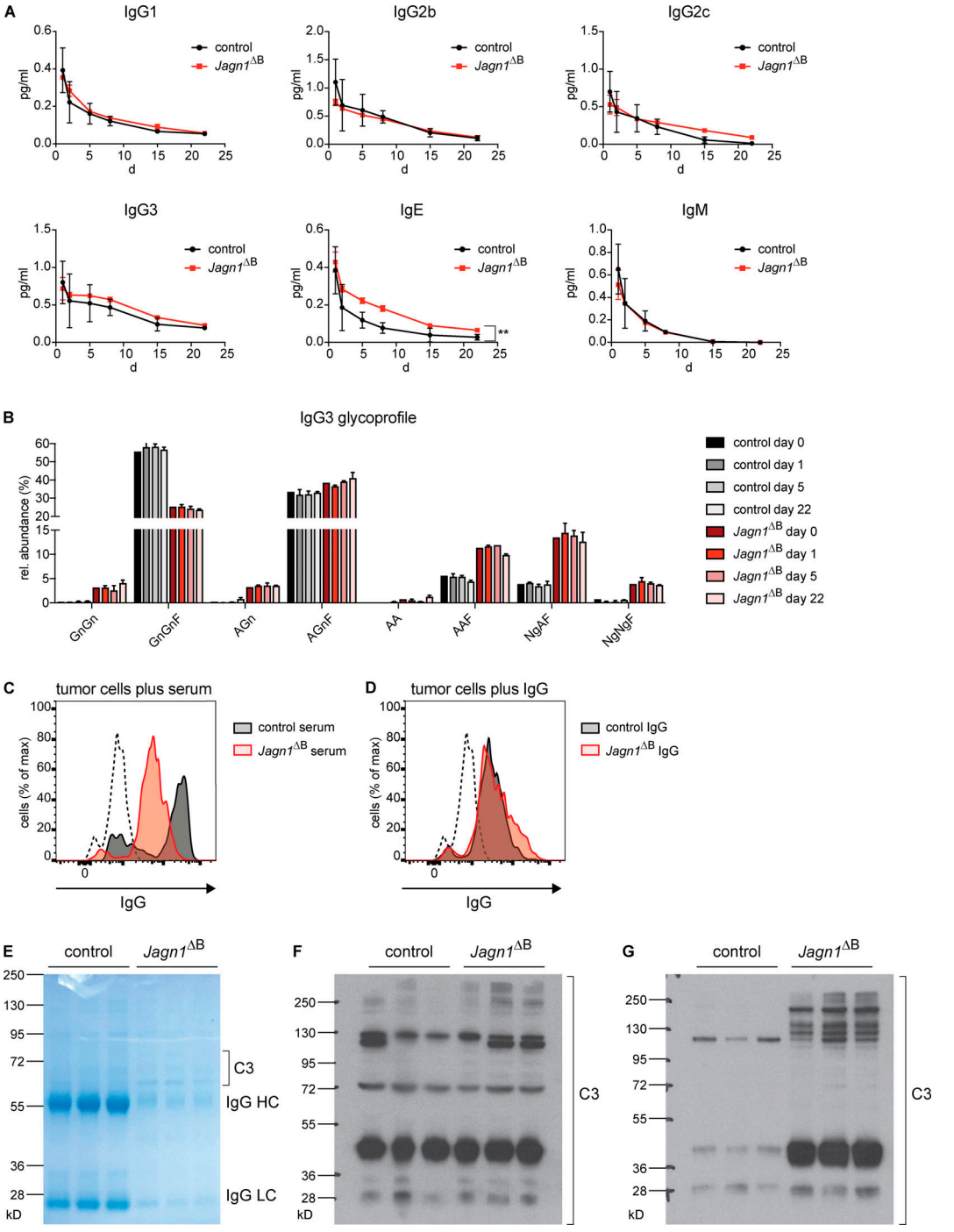

Figure S5. **Unchanged in vivo stability and target cell binding of *Jagn1*$^{\Delta B}$ mouse serum–derived Ig, but increased complement component 3 (C3) binding to antibodies from *Jagn1*$^{\Delta B}$ mice. (A)** Ig concentrations in sera from *Rag2*$^{-/-}$ mice infused with sera from control and *Jagn1*$^{\Delta B}$ mice. Sera were normalized to contain equal amounts of IgG. Ig levels were measured for 3 wk following serum transfer by an isotype-multiplexing assay (n = 3). Data are shown for one of two independent experiments. **(B)** Relative abundance of IgG3 glycoforms in mice transferred with sera from donor mice of the indicated genotypes as measured with LC-ESI-MS on day 1, 5, and 22 after the serum transfer (day 0, n = 1; day 1, 5, and 22, n = 3). IgG3 glycoforms are abbreviated according to the ProGlycan nomenclature denoting the terminal residues of the two chains. **(C and D)** Representative histogram overlays (corresponding to Fig. 5, G and H) to illustrate IgG binding to E0771 tumor cells incubated with control and *Jagn1*$^{\Delta B}$ mouse sera (C) or purified IgG (D) as assessed by cell surface staining for IgG using flow cytometry. The dotted line in the histogram represents background controls, adding the secondary antibody only. Data are shown for one of two independent experiments. **(E)** Coomassie staining of a protein gel loaded with sera after Ig purification by protein G beads from three individual control and *Jagn1*$^{\Delta B}$ mice. HC, heavy chain; LC, light chain of IgG. A representative gel is shown for one of three independent experiments. **(F)** Immunoblot analysis of control and *Jagn1*$^{\Delta B}$ mouse sera to assess the protein expression of complement C3. Data from individual mice are shown for one of two independent experiments. **(G)** Immunoblot analysis of control and *Jagn1*$^{\Delta B}$ mouse sera after Ig purification by protein G beads to assess antibody-bound complement C3 in three individual mice. A representative blot is shown for one of two independent experiments. Panel A was analyzed by two-way ANOVA with Bonferroni correction. **, P < 0.01. Error bars represent means ± SD.

Provided online are two tables as Excel files. Table S1 lists primers used for genotyping and gene expression analysis in this study, and Table S2 provides details of the antibodies used in this study.